

Scanning acoustic microscopy and its applications to material characterization

Zuliang Yu

Laboratory of Information Technology, University of Hannover,
D-30167 Hannover, Germany

Siegfried Boseck

Department of Physics, Institute of Material Science and Structure Research,
University of Bremen, D-28334 Bremen, Germany

The scanning acoustic microscope is a powerful new tool for the study of the physical properties of materials and has been successfully used for imaging interior structures and for nondestructive evaluation in materials science and biology. Its principles of operation, resolution, penetration ability, and contrast mechanisms are simply described in this paper. Recent progress in the application of acoustic microscopy to material characterization in solid materials is summarized. The experimental elastic microanalysis of bulk materials is carried out by measuring $V(z)$, which includes examining the reflectance function of solid material, measuring the phase velocity and attenuation of leaky surface acoustic waves at the liquid-specimen boundary, and determining the elastic constants of the material. The layer thickness and mechanical properties of layered solids are studied by examining the dispersion properties of surface acoustic waves. A knowledge of the propagation properties of acoustic waves on the surface of materials is essential for understanding the contrast mechanisms and quantitative measurements in acoustic microscopy; these propagation properties are thus also briefly described in this paper. Finally, further developments of the scanning acoustic microscope aimed at improving its performance for quantitative evaluation are presented. These could expand the scope of the acoustic microscope as a diagnostic tool in many areas of science and technology.

CONTENTS

I. Introduction	863	2. Layer-thickness measurement in a two-layered structure	882
II. General Description of the Scanning Acoustic Microscope	864	3. Measurement of mechanical properties in a layered structure	883
A. Transmission and reflection types of scanning acoustic microscopes	864	VI. Further Developments in Scanning Acoustic Microscopy	883
B. Principles of the reflection scanning acoustic microscope	865	A. Specialized lens geometries	883
C. Resolution of the acoustic microscope	866	1. Line-focus-beam lens	884
D. Interior imaging and penetration ability	866	2. Lamb-wave lens	884
III. Contrast Mechanisms in the Scanning Acoustic Microscope—The $V(z)$ Effect	867	B. Scanning alternatives and recorded functions	884
A. The $V(z)$ curve	867	1. $V(f)$ function	885
B. Theory of $V(z)$	868	2. $V(\theta)$ function	885
1. Rayleigh surface waves in a nonlayered solid	869	VII. Summary	885
2. Ray optical model	870	Acknowledgments	887
3. Fourier optics model	870	Appendix A: Acoustic Field $u_1(\theta)$ at the Back Side of the Lens and Generalized Pupil Function $P(\theta)$	887
IV. Elastic Microanalysis by $V(z)$ Measurement	873	1. Acoustic field $u_1(\theta)$ at the back side of the lens	887
A. Examination of the reflectance function	873	2. Generalized pupil function $P(\theta)$	888
B. Measurement of phase velocity of surface acoustic waves	873	Appendix B: Formulation of Reflectance Function $R(\theta)$ in a Multilayered Solid	888
C. Measurement of attenuation of surface acoustic waves	873	References	890
D. Determination of elastic constants of bulk materials	874		
V. Material Characterization of a Layered Solid by Acoustic Microscopy	875		
A. Dispersion of surface acoustic waves in a layered solid	875		
B. Behavior of $V(z)$ for a layered structure	878		
1. Multiple-ray interference model of $V(z)$	878		
2. Wave-form analysis of the $V(z)$ curve	878		
C. Material characterization of a layered solid by surface acoustic wave dispersion	881		
1. Layer-thickness measurement in a single-layered structure	881		

I. INTRODUCTION

In materials science and biology the microscope has proven to be one of the most powerful of scientific tools. The optical microscope and the electron microscope have given us extraordinary insights into the world of the extra small, and they will surely continue to enjoy widespread use in the future. The field of microscopy as a whole has historically developed by adding new classes of radiation. So far, we have seen the development of the infrared microscope, scanning Auger microscope, Raman microscope, scanning laser microscope, ion microscope, x-ray microscope, tunneling microscope, and the list seems to be growing all the time. All of these microscopes have their special characteristics, their particular advantages and limitations, and they should be

viewed as a complementary collection. The scanning acoustic microscope (SAM) is a new member of this collection, and it would appear to be one of the most promising members for the study of the elastic properties of materials.

The concept of acoustic microscopy was first put forward by Sokolov in 1949. Unlike other forms of radiation, an acoustic wave interacts directly with the elastic properties of the material through which it propagates. The wavelength of sound at a high frequency can be very short, from which it should be possible to build an acoustic microscope with a resolution comparable to that of the optical microscope. However, until the early 1970s this was not achieved because techniques for producing high-frequency sound waves were not readily available. Since the 1970s the acoustic microscope has undergone many improvements. The greatest improvement, the scanning acoustic microscope, was developed at Stanford University under the direction of C. F. Quate (1985). Now, various commercial acoustic microscope instruments are available in countries such as Japan, England, and Germany for scientific and industrial applications.

Characterization of near-surface properties of materials is an important test of their structural integrity. Nondestructive evaluation of these properties is usually carried out using acoustic techniques. Surface acoustic waves (SAWs) are frequently used for this purpose, because they are spatially confined to the surfaces of materials and very sensitive to surface inhomogeneities. Several techniques can be used to excite focused surface acoustic waves on the surface of materials for imaging purposes; of these, scanning acoustic microscopy is unique in its image quality and resolution. Compared to other techniques of microscopy, scanning acoustic microscopy provides a combination of features that make it valuable for a wide range of applications. It is possible to use it to characterize the properties of materials on a microscopic scale: subsurface image of the material structures can be obtained due to the ability of ultrasonic waves to penetrate materials that are opaque to other kinds of radiation; the elastic constants of bulk materials, and the phase velocity and attenuation of leaky surface acoustic waves excited on the surface of specimens can be quantitatively examined through $V(z)$ measurements; important mechanical properties like elastic constants and residual stresses, adhesion properties, and film thickness in layered structures can also be evaluated from dispersion properties of surface acoustic waves examined by acoustic microscopy.

Although the technique of scanning acoustic microscopy was introduced many years ago and a number of articles and reviews have been published (Lemons and Quate, 1974, 1979; Quate *et al.*, 1979; Wilson and Weglein, 1984; Briggs, 1985, 1992), it is still not familiar to many physicists due to the limited number of instruments worldwide. To show the spectrum of its applications, this paper presents a brief review of scanning acoustic microscopy and its applications to material characterization. The first part of the article is devoted to a general description of the scanning acoustic microscope, which includes principles of operation, resolution, penetration ability, and contrast mechanisms. The second part is concerned with the applications of acoustic microscopy to material characterization in solid materials. Our emphasis is on quantitative evaluation. The interior imaging of a

material subsurface and applications in biology will be omitted, as they can be found elsewhere (e.g., Hoppe and Bereiter-Hahn, 1985; Miller, 1985). In acoustic microscopy, surface acoustic waves such as Rayleigh waves and Sezawa waves (generalized Lamb waves) can be excited and received by the acoustic microscope; the interference of these waves plays a very important role in imaging and quantitative measurements made with acoustic microscopy. Knowledge of surface acoustic wave propagation is not as widespread among technical people as is knowledge of light wave propagation, and as a result the contrast mechanisms of the SAM and its applications are not widely understood. Therefore we shall briefly describe the propagation properties of surface acoustic waves in nonlayered and layered structures, and then present their behaviors in acoustic microscopy. Finally, in the present paper we also indicate some limitations of the conventional scanning acoustic microscope, which is equipped with a spherical lens, for material characterization, and point out development trends in lens constructions and alternative types of scanning for the scanning acoustic microscope.

II. GENERAL DESCRIPTION OF THE SCANNING ACOUSTIC MICROSCOPE

The development of the scanning acoustic microscope is based on the realization that one cannot make a high-resolution acoustic lens that can image more than one point of an object at a time, but it is possible to make an acoustic lens that has excellent focusing properties on its axis. In order to build up an image, the specimen is mechanically scanned in the common focal plane of the lens and a scanned image can be obtained, in a manner similar to scanning electron microscopy or to domestic television. It is the use of mechanical scanning that simplifies the lens design and operation, i.e., the lens need perform well only on axis, and has made it possible to record high-quality acoustic images with submicrometer resolution.

A. Transmission and reflection types of scanning acoustic microscopes

In the scanning acoustic microscope both the illumination and the detection are performed by focusing acoustic lenses and, since these are focused at the same point, the configuration may be described as confocal. The image of material properties can be recorded either in reflection or transmission. If the illumination and the reception of the acoustic waves are performed by two identical lenses arranged confocally, the SAM is called a transmission SAM. The lens geometry used for transmission imaging is shown schematically in Fig. 1 (Lemons and Quate, 1979). This geometry consists of a symmetrical pair of lens elements connected by a small volume of liquid. Each lens consists of a single spherical interface between the liquid and a lens rod. The lens element is formed by polishing a small concave spherical surface in the end of a sapphire rod. At the opposite end of the rod a thin film piezoelectric transducer is centered on the axis of the lens surface.

In the reflection SAM, the transmission arrangement is conceptually folded over, so that the same lens is used for

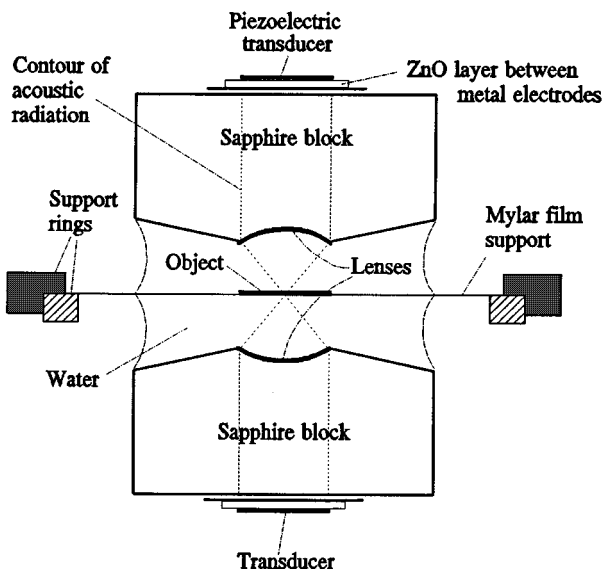


FIG. 1. Lens geometry of the transmission acoustic microscope.

both transmitting and receiving the acoustic signal (see Fig. 2). The transmission version can use a simple continuous wave, but in the reflection mode pulsed signals should be used in order to separate the reflected signal from the transmitted signal. In the transmission mode the ultrasonic beam passes through the object placed between the objective and collector, and since the acoustic microscope has a sharply defined depth of field, the image of a thin layer cut out from the interior of a specimen may be obtained. The transmission acoustic microscope is especially suitable for investigation of samples with acoustic impedances and attenuation comparable to those of water, i.e., for biological specimens. The reflection mode is more promising for the investigation of samples of high acoustic impedance and attenuation, i.e., for solid materials. The operation of a transmission SAM requires the lenses to be set up so that they are accurately confocal, which becomes difficult with high frequencies and shorter wavelengths. In the reflection SAM the need to adjust the lenses to be confocal is obviated. Specimens to be im-

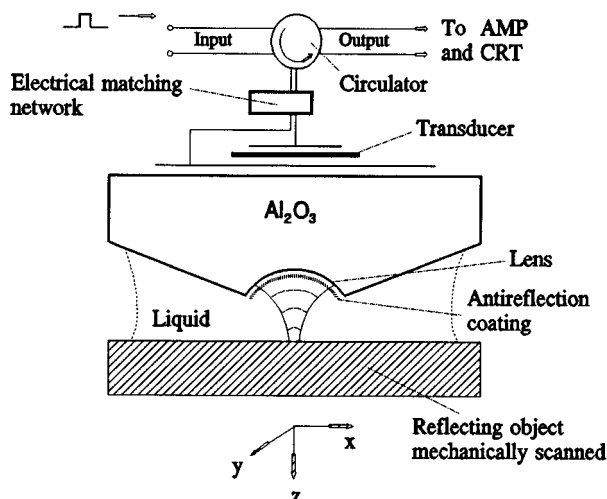


FIG. 2. Schematic representation of a reflection SAM.

aged in the transmission version must be thin in order to enable acoustic waves to propagate through specimens. For biological specimens, this often presents few problems, but for many solids such a thin specimen is quite difficult to prepare. Therefore, although the first scanning acoustic microscope operated in transmission, there is an increasing shift from transmission microscopy to reflection microscopy. Most of the recent development and application of the SAM has been with the reflection mode. In this paper only the reflection scanning acoustic microscope will be described.

B. Principles of the reflection scanning acoustic microscope

The scheme of a reflection scanning acoustic microscope is shown in Fig. 2. The heart of it is an acoustic lens, which is a sapphire rod cut along the crystallographic c axis of the sapphire. In the center of one face of the rod a concave spherical surface is ground. This surface provides the focusing action and, to optimize transmission of the acoustic waves, it is coated with a quarter-wavelength-thick matching layer. On the other face of the rod a piezoelectric transducer is deposited, usually a thin film of rf-sputtered ZnO. In use, a coupling fluid (usually water) is necessary between the lens and the specimen. When the transducer is energized with a short rf pulse (approximately 30 ns in duration), plane acoustic waves are generated, which travel through the rod and are focused on the axis of the lens by refraction at the spherical interface between the lens and the liquid. The object to be imaged is placed at the focus of this lens. The acoustic waves are partially reflected at the interface and the echoes thus produced traverse the system in reverse order and are converted back into an electrical pulse by the transducer, which acts in this case like a light-sensitive receptor and coherent detector. The strength of this pulse is proportional to the acoustic reflectivity of the object at the point being investigated. By mechanically scanning the object in a raster fashion, one can build up an acoustic image of the desired field of view and display it on a TV monitor.

In optics a complex compound objective lens for microscopes with high numerical aperture is needed to compensate accurately for both geometrical and chromatic aberrations. In acoustics this is neither possible nor necessary. The simple acoustic lens shown in Fig. 2 has been capable of producing perfect diffraction-limited images. The reason is as follows. First, chromatic aberrations do not arise in the acoustic microscope because in its usual mode of operation it may be considered essentially monochromatic. Secondly, as acoustic imaging is always done on axis, spherical aberration is the only possible source of aberration. In geometrical optics spherical aberrations are calculated using third-order theory, whose magnitude is proportional to D/n^2 (Lemons, 1975), where D is the lens aperture and n is the relative refractive index. In the optical case $n \sim 1.5$ for glass, so that spherical aberration is large and important, whereas in the acoustic case the velocity of sound along the c axis in sapphire is 11,100 m/sec and in water it is about 1,500 m/sec. This means that there is a very large refractive index ($n = 7.4$) for acoustic waves striking the lens, which is much greater than would be encountered in any comparable optical system.

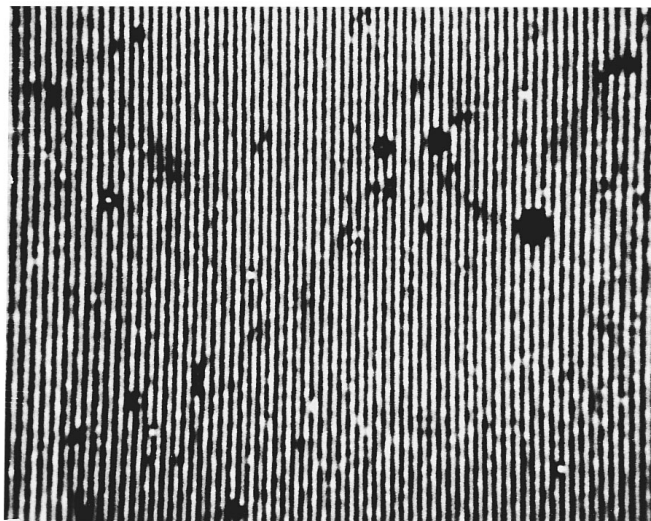


FIG. 3. Resolution test of a grating of $0.4 \mu\text{m}$ period imaged at 2.0 GHz, at 60°C (Leica, Wetzlar).

Further spherical aberration scales down with smaller- D (higher-frequency) lenses. As a consequence, a single small lens surface can provide a high-aperture acoustic lens with aberrations considerably less than a wavelength.

C. Resolution of the acoustic microscope

Since the aberrations in the acoustic microscope are negligible, the resolution of an acoustic lens is determined almost solely by diffraction limitations, and is $R = 0.51\lambda_w / \text{N.A.}$ (Kino, 1987), where λ_w is the wavelength of sound in liquid, and N.A. is the numerical aperture of the acoustic lens. For smaller (high-frequency) lenses, N.A. can be about 1, and this would give a resolution of $0.5 \lambda_w$. Thus a well-designed lens can obtain a diameter of the focal spot approaching an acoustic wavelength (about $0.4 \mu\text{m}$ at 2.0 GHz in water). The resolution of an acoustic microscope may be tested by imaging a specimen with a fine grating ruled on it. Figure 3 shows an acoustic image of an optical grating with a period of $0.4 \mu\text{m}$ at 2.0 GHz. In this case the acoustic microscope can achieve a resolution comparable to that of the optical microscope.

As the resolution is proportional to the wavelength in the liquid λ_w , the way to improve the resolution is therefore to make the wavelength smaller. The wavelength depends on the velocity of sound in the liquid, ν_w , and the frequency f such that $\lambda_w = \nu_w / f$. That is, if the frequency could be indefinitely increased, unlimited resolution could be achieved. Unfortunately, the application of higher frequencies is restricted due to the attenuation of the coupling medium and the available radius of curvature of the lens. Acoustic waves need a medium to support their propagation (in acoustics there is no analogy to a vacuum in optics). Between the acoustic lens and the specimen the medium must be a liquid, in order to permit scanning. Most liquids at or near room temperature exhibit linear viscosity, which causes the attenuation of acoustic waves propagating through them to be proportional to the frequency squared. To increase the frequency, it is necessary to reduce the liquid path length

between the lens and the specimen, which means that the focal length of the lens and in turn its radius of curvature must be small. Grinding lenses with very small radius is a quite difficult art. Moreover, even if it is possible to grind lens radii as small as required (about 15 microns), for a lens operating in a pulsed mode with higher frequencies, there are major problems with high-speed switches to obtain sufficiently narrow pulses to prevent the specimen from being swamped by the lens echo. Usually, the highest frequency for a microscope with water coupling at 60°C is about 2 GHz.

The attenuation of acoustic waves in water decreases with increasing temperature. By raising the temperature of the water it is possible to reduce the attenuation. Using this feature, and by stretching the existing technology to its limits, the reflection SAM has been operated in water at 3.5 GHz, with a corresponding wavelength of $0.425 \mu\text{m}$ (Rugar, 1981). The utilization of the nonlinear properties of the coupling liquid has been proposed to enhance resolution. The generation of harmonics makes possible an improvement in the resolution of the microscope by at least a factor of 1.4 (Rugar, 1984). Finding a liquid that has a lower velocity, a lower absorption coefficient, or preferably both, further improves the resolution. One possibility is to use cryogenic fluids such as superfluid helium. In liquid helium at 0.1 K, sound velocity is equal to 238 m/sec, and attenuation is so small that it becomes negligible. In this type of cryogenic SAM, operating with 8 GHz frequency, the resolution of micrographs obtained was better than $0.025 \mu\text{m}$ (Hadimioglu and Foster, 1984). At this level, cryogenic acoustic microscopy as a research tool may offer an alternative to electron microscopy.

D. Interior imaging and penetration ability

The ability to image below the surface of solids is another attractive property of the acoustic microscope. Many materials that are opaque to light are transparent to acoustic waves. This property of acoustic waves has long been exploited in ultrasonic nondestructive testing. Indeed, due to this ability acoustic microscopy provides valuable insights regarding material structures and subsurface imaging which cannot be obtained any other way. Figure 4 shows a typical example of what can be achieved by employing the SAM for subsurface imaging. It is an acoustic reflection imaging of a 5-DM German coin at 10 MHz. The penetration ability is quite remarkable. By appropriately choosing the focal position of the acoustic image, it is possible to show clearly the front and back pictures. Figure 5 shows a comparison between the optical and the acoustic images of a Kelvin contact with aluminum top surface on silicon in semiconductor technology. In the optical image the contact appears to be homogeneous, whereas in the acoustic image a defect in the contact is visible. An acoustic microscope used in such studies is capable of revealing defects beneath the surface metallization which are hard to detect using other techniques.

The penetration ability of a SAM can be estimated as equal to the penetration of excited surface waves, which is about the same magnitude as the wavelength of the surface waves. The practical penetration depth depends on the elastic parameters of the object, the signal-to-noise ratio, and the operating frequency of the acoustic microscope (Atalar,



FIG. 4. An acoustic image of a 5-DM German coin at 10 MHz (Leica, Wetzlar).

1985). A higher acoustic mismatch between the object and liquid will lower the penetration depth, and a higher signal-to-noise ratio will improve it. Some changes in the parameters of the acoustic lens system, such as optimizing the lens opening angle, can maximize penetration for a given material. On the other hand, increasing the operating frequency improves the resolution, but reduces the penetration due to the increase in attenuation with frequency. Trade-offs between resolution and penetration depth must be made for acoustic microscope instruments. At the moment the most promising frequency range for subsurface imaging analysis would appear to be 10–150 MHz, where penetration up to a few mm is easily attained. Table I gives practical resolution limits and penetration depths for copper and brass with a SAM (Block *et al.*, 1989).

III. CONTRAST MECHANISMS IN THE SCANNING ACOUSTIC MICROSCOPE—THE $V(z)$ EFFECT

The traditional microscopist is interested in resolution. The acoustic microscopist may have that interest. However, the significance of the scanning acoustic microscope does not lie in its resolution alone. There is a stronger interest: image contrast. In acoustic microscopy the near-surface of the specimen is examined, and therefore the acoustic image contains information about the way that acoustic waves interact with the properties of the specimen. Image contrast observed in acoustic microscopy can be related to the elastic properties at the surface as well as below the surface of the sample. Thus there is a special feature that is not shared with any other kind of microscopy. That is, fringes are seen which are an interference effect associated with waves that can be excited in the surface of specimen. Interpretation of the contrast of these fringes is not a simple matter. One cannot sim-

ply say that a brighter area corresponds to a higher (or lower) density, or to a greater (or smaller) elastic modulus. Moreover, the contrast varies very sensitively with the distance between the lens and the surface of the specimen. This behavior is best visualized as a $V(z)$ curve. The $V(z)$ effect is a “source of contrast” and is used to record quantitative information on the elastic properties of a specimen with microscopic precision. The understanding of the $V(z)$ effect in the SAM is, for a microscopist, of great significance.

A. The $V(z)$ curve

As mentioned above, by mechanically scanning the object plane one can obtain the scanning image of a specimen at the surface or subsurface of an object. Rather than scan in the plane, one keeps the lens and object at a fixed (x, y) position and translates the lens towards the object in the z direction; one then observes a series of oscillations in the transducer video output as a function of z . This dependence of the variation of the signal output, V , on the defocus z is known as the acoustic material signature or simply $V(z)$ curve. Historically the study of this effect was pioneered experimentally by Weglein and co-workers (Weglein, 1979a) and theoretically by a number of authors (Atalar, 1978; Wickramasinghe, 1979). This effect gives the acoustic microscope an important edge over the optical microscope.

The theory of $V(z)$ will be considered in the next section. Here it is first helpful to give a general structural decomposition of the $V(z)$ curve. An experimental $V(z)$ curve for a quartz specimen, obtained with a commercial instrument known as the Ernst Leitz scanning acoustic microscope (ELSAM),¹ is shown in Fig. 6, illustrating some of the main features of $V(z)$. An experimental $V(z)$ curve is often plotted with a logarithmic V axis. This can cause the minima to appear as very pronounced nulls. All $V(z)$ curves presented in this paper are also normalized for clarity and ease of comparison.

First there is the strong central maximum, centered on the focal plane ($z \approx 0$), which is a characteristic of the sample-immersion liquid interface and due to the existence of the primary reflection. This region does not depend on the material properties of the sample being measured. Secondly the curve for positive z attenuates rapidly with increasing distance z because in this region the sample surface is farther away than the focal plane, much of the acoustic energy is reflected outside the lens, and only a less convergent beam is received by the transducer. On the negative z side there are strong oscillations, where a series of periodic maxima and minima occurs, characterized by a period Δz . This region is characteristic of the sample's acoustic properties; the patterns vary with the material, as do the depths of the minima and the relative magnitudes of the maxima. As shown below, Δz may be multivalued or may vary with z for a layered solid. This portion contains the material-dependent informa-

¹The ELSAM is a reflection-type, water scanning acoustic microscope, designed for $V(z)$ measurement with continuously tunable operation in the frequency range 0.8–2.0 GHz. For this frequency range, spherical acoustic lenses with a radius of curvature of 40 μm and an opening of 100° are used.

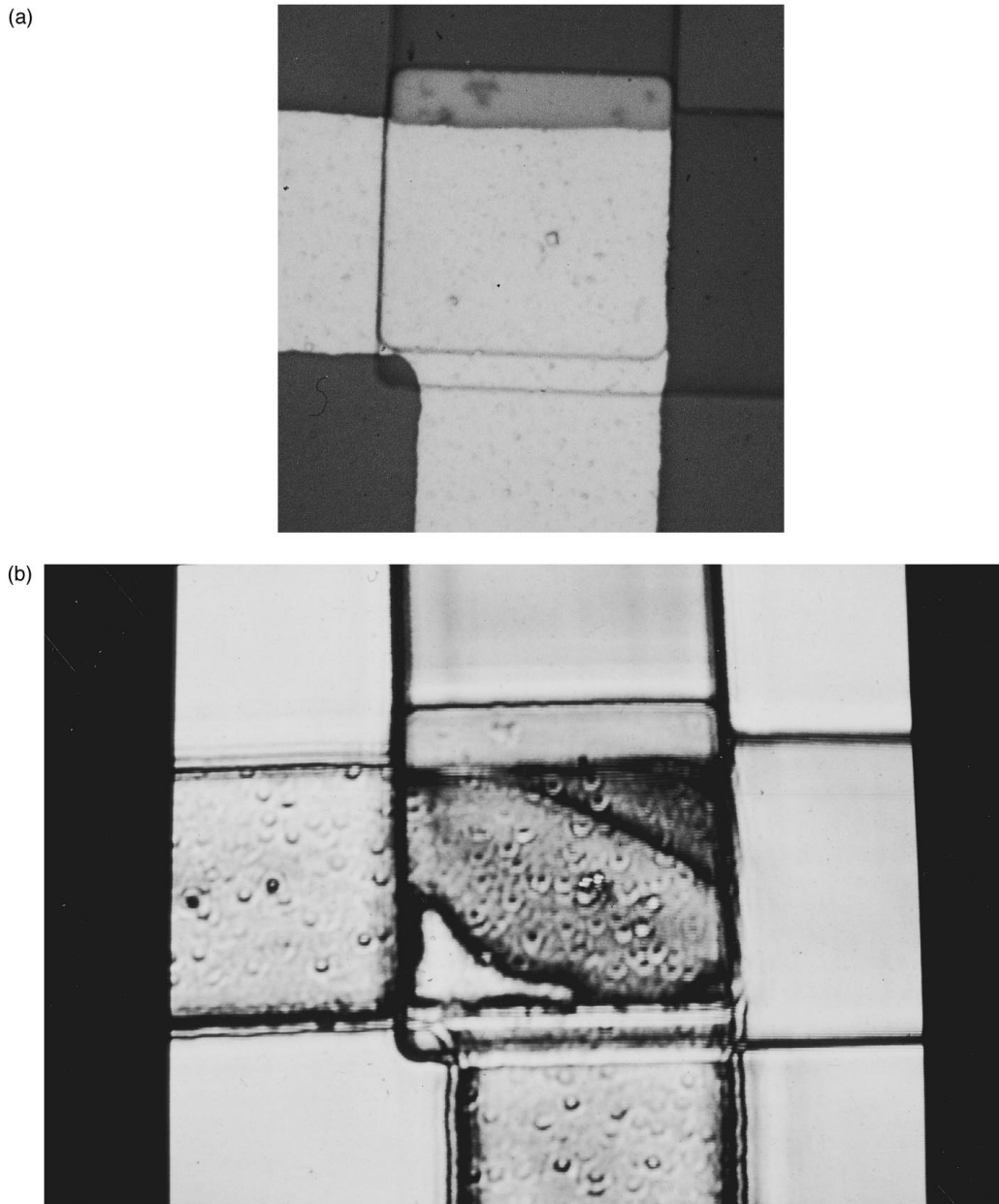


FIG. 5. Images of a Kelvin contact: (a) optical image; (b) acoustic image of the same sample at 1.4 GHz.

tion and is referred to as the acoustic material signature, from which an important method for the nondestructive evaluation of material properties was developed. It should be pointed out that in this figure the $V(z)$ curve is superimposed by a

“water ripple” and an obvious fluctuation occurs over the entire region of the curve. A “water ripple” is a short period oscillation due to the coupling liquid, which results from interference between internal lens reflections and the normally reflected component of the signal. By use of an appropriate low-pass filtering technique, the effect of “water ripple” can be easily minimized.

TABLE I. Practical resolution limits and penetration depth in a SAM.

Operation frequency	Resolution limit	Penetration depth
20 MHz	100 μm	4 mm
200 MHz	8 μm	300 μm
1000 MHz	1.5 μm	25 μm
2000 MHz	0.7 μm	10 μm

B. Theory of $V(z)$

$V(z)$ is an interference effect between surface waves, which are excited in the specimen and often referred to as Rayleigh waves, and specularly reflected waves. To interpret this effect it is first necessary to say a little about Rayleigh waves.

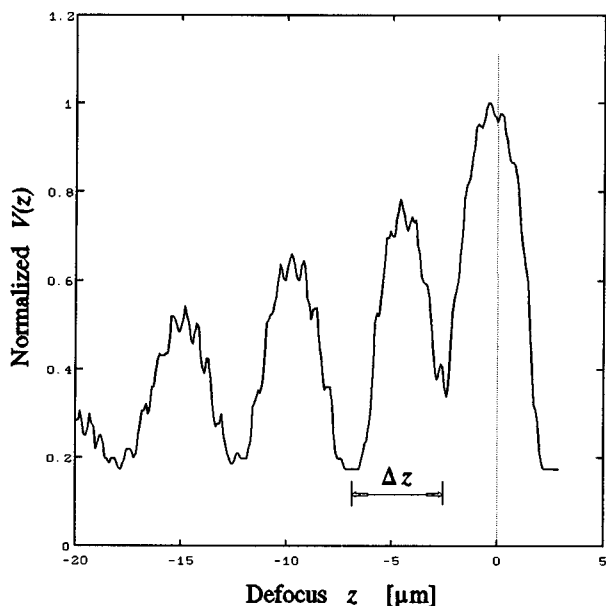


FIG. 6. An experimental $V(z)$ curve with water ripple at 1.8 GHz, at 60°C. This was obtained with an Ernst Leitz scanning acoustic microscope (ELSAM).

1. Rayleigh surface waves in a nonlayered solid

The propagation of acoustic waves in a solid is more complicated than in a liquid. In a liquid sound travels as a longitudinal wave. In a solid propagation properties can be described by the Christoffel equations, which show that three kinds of elastic waves can be propagated (Auld, 1973). One of these corresponds to a longitudinal wave, and the other two are degenerate shear waves with orthogonal polarizations. Another kind of acoustic wave can occur on the surface of a solid. This is a Rayleigh surface wave (Rayleigh, 1885). A Rayleigh surface wave is a mode of propagation of elastic energy along the free surface of a solid in which the displacement amplitudes of the propagating wave decay in an exponential fashion with depth beneath the surface, so that essentially all of the associated energy density is concentrated within a distance of the order of a wavelength below the free surface. The particle motion in a Rayleigh surface wave is an ellipse, the principal axes of which are parallel and perpendicular to the boundary (see Fig. 7). Rayleigh waves in nonlayered solids are nondispersive, and their velocity ν_R is approximately related to the shear bulk wave velocity β_{solid} as (Scruby *et al.*, 1987)

$$\nu_R \approx (1.14418 - 0.25771\sigma + 0.12661\sigma^2)^{-1} \beta_{\text{solid}}, \quad (1)$$

where σ is the so-called Poisson ratio. If the solid is anisotropic, say a single crystal, the Rayleigh wave still exists for any given direction of propagation, but the detailed properties differ from the isotropic case; for example, the ellipse traced out by the surface particle displacement need not be normal to the surface, and the decay of amplitude with depth can be oscillatory. Moreover, these properties, and in particular the phase velocity, depend on the direction of propagation relative to the crystal axes. In this paper we shall consider only the propagation properties of surface waves in isotropic materials.

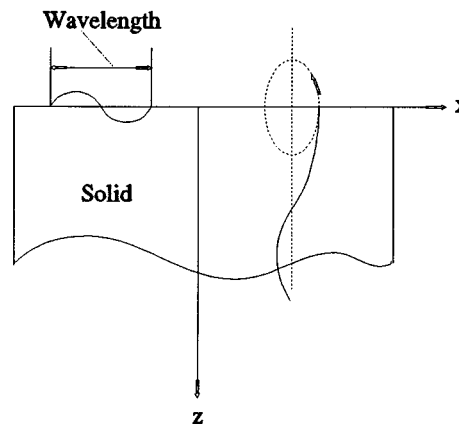


FIG. 7. Schematic drawing of a Rayleigh wave.

If the solid material is immersed in a liquid, a Rayleigh-like surface wave may be generated at the liquid-solid interface. The phenomenon consists of a resonant energy transfer between the longitudinal wave in the liquid and the Rayleigh-like wave on the liquid-solid interface. This Rayleigh-like surface-wave excitation differs from the classical Rayleigh wave in that the energy is continuously “leaking” away from the solid region to the liquid region. The surface wave generated is evanescent; it will eventually leak back into the liquid medium as a bulk wave. Moreover, the surface waves start leaking as soon as they are generated. Since the energy leaks into the liquid, this surface wave is called a leaky Rayleigh wave. The leaky-Rayleigh-wave velocity is slightly ($\sim 0.1\%$) different from that of the solution given by Eq. (1) because of the presence of liquid (Chimenti *et al.*, 1982).

When an acoustic beam is incident on the liquid-solid interface at the Rayleigh angle, which is the angle that satisfies Snell’s law,

$$\theta_R = \sin^{-1}(\nu_w / \nu_R), \quad (2)$$

where ν_w is the sound velocity in the liquid and ν_R is the phase velocity of the leaky Rayleigh wave, it exhibits two significant features: Schoch (lateral) displacement Δ_s (Schoch, 1950, 1952) and associated distortion of a finite-aperture incident beam. By “Schoch displacement” one means that a beam of sound undergoes a relatively large lateral displacement at reflection from a solid surface, if an angle of incidence is chosen such that a Rayleigh wave is excited in the solid medium. Such a lateral shift for an optical beam is known as the “Goos-Hänchen shift” (Goos and Hänchen, 1947). These effects typically lead to a bimodal reflected acoustic field, and the reflected beam is split into two components: a specular beam (specular reflection) and a nonspecular beam displaced a distance laterally (nonspecular reflection); see Fig. 8. The leaky Rayleigh wave will radiate leaks into the liquid and, combined with a specularly reflected wave, will produce a so-called “null strip.”

The theory of $V(z)$ has been derived in two different ways: those involving Fourier angular spectrum analysis (Atalar, 1978; Wickramasinghe, 1979) and those based on a ray optical model (Bertoni, 1984). Both models are of importance for explaining the $V(z)$ effect.

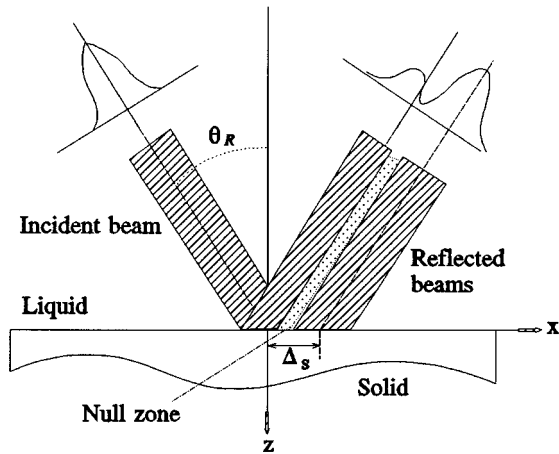


FIG. 8. Reflection of finite beam from liquid-solid interface at the Rayleigh angle.

2. Ray optical model

From the analogy of $V(z)$ curves to effects in physical optics, it is natural to consider the $V(z)$ effect as a result of acoustic ray interference. Consequently, a physical model of the $V(z)$ effect has been proposed, which essentially regards $V(z)$ as the interference between two families of acoustic rays; see Fig. 9. One component, A , is a family of specularly reflected acoustic rays at almost normal incidence from the surface of the specimen. The second component, B , is a family of laterally displaced leaky Rayleigh waves (non-specular reflection), symmetrical to the incident beam. These two beams, A and B , arrive at the transducer and produce an output signal. Then interference effects between them are observed.

We call this kind of ray model a double-ray interference model because two families of ray components were taken into account. The interference of rays with differing paths gives the period Δz of the resulting oscillations in $V(z)$ as follows. Compared with focus F the normal ray undergoes a change in path length of z (the defocus distance) before being reflected, and a further amount z on the return journey,

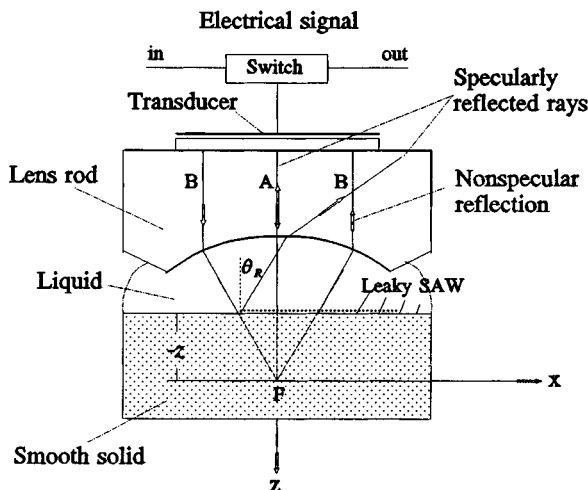


FIG. 9. Double-ray interference model of $V(z)$.

i.e., a total change in path length of $2z$. The ray incident at the Rayleigh angle has its path in the liquid shortened by $z \cdot \sec \theta_R$, and then excites a Rayleigh wave on the specimen surface. This propagates along the surface, leaking a wave back into the liquid, and the ray symmetrically placed with respect to the incident ray travels back to the lens with its path also shortened by $z \cdot \sec \theta_R$. The path length traveled by the Rayleigh wave on the surface of the specimen this is equivalent to an acoustic path in the liquid of $2z \cdot \tan \theta_R \cdot \sin \theta_R$, by Snell's law. There is also a phase change of π associated with the excitation and re-radiation of the Rayleigh wave. The phase difference between the two rays (assuming that the lens eliminates all other phase difference) is

$$\begin{aligned} \Delta \phi &= (2z - 2z \sec \theta_R + 2z \tan \theta_R \sin \theta_R) k_w + \pi \\ &= 2z [1 - \sec \theta_R (1 - \sin^2 \theta_R)] k_w + \pi \\ &= 2k_w z (1 - \cos \theta_R) + \pi, \end{aligned} \tag{3}$$

where $k_w = 2\pi/\lambda_w$ is the wave number of sound in the liquid, and λ_w is the wavelength of sound in the liquid.

These two beams, A and B , arrive at the transducer and therefore produce an output signal. Based on the interference principle of double rays in physical optics, an interference pattern occurs in the $V(z)$ response of the transducer. A phase change of 2π in the relative phase difference corresponds to a dip interval Δz in the $V(z)$ curve. Using Eq. (3) and ignoring the constant phase term π , we get oscillations of periodicity

$$\Delta z = \frac{2\pi}{2k_w(1 - \cos \theta_R)} = \frac{\lambda_w}{2(1 - \cos \theta_R)}. \tag{4}$$

Equation (4) for the periodicity of the oscillations in $V(z)$ is of fundamental importance, and must be understood by every acoustic microscopist.

From the user's point of view, it is more appropriate to rewrite Eq. (4) by use of Eq. (2) and the measurable quantities, frequency f and Δz , to yield the Rayleigh velocity ν_R (Weglein, 1985), i.e.,

$$\nu_R = \frac{\nu_w}{[1 - (1 - \nu_w / (2f\Delta z))^2]^{1/2}}. \tag{5}$$

This simple ray optics theory allows quantitative measurement of the phase velocity of a leaky Rayleigh wave from the $V(z)$ curve, and characterization of the acoustic properties of materials.

3. Fourier optics model

The other way to interpret the $V(z)$ effect is the Fourier angular spectrum technique, which is based on the well-known theory of Fourier optics and can be easily manipulated mathematically. By decomposing the acoustic field distributions at the various planes in the acoustic microscope system into angular spectrums of plane waves, it is possible to arrive at an integral expression for $V(z)$ (Atalar, 1978; Wickramasinghe, 1979). But, this model may be derived in a simpler form following Sheppard and Wilson (1981). Figure 10 shows the same acoustic imaging system as shown in Fig.

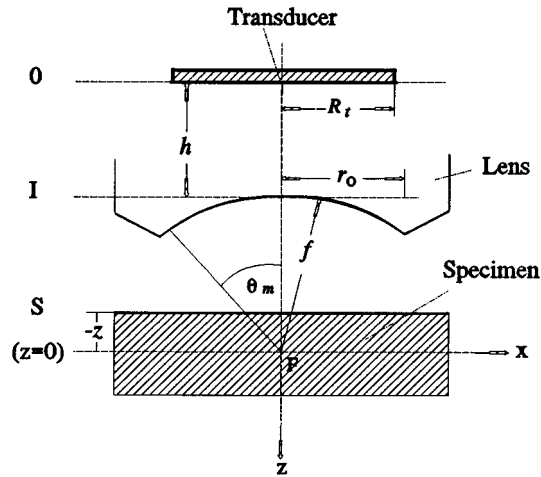


FIG. 10. Geometry and coordinate system used for analyzing acoustic field distributions: Plane 0, transducer plane; plane I, back side plane of the lens; plane S, surface plane of the tested object; plane $z=0$, focus plane; R_t , radius of the transducer; r_0 , radius of the lens aperture; θ_m , semiangle of the lens; h , distance between the transducer and the lens; f , local distance of the lens; F , focused point.

2, and its coordinate system used for analysis of the acoustic field distributions. A plane wave of unit amplitude is generated by the transducer, which propagates through a distance h until it encounters the lens at the sapphire-liquid interface. The acoustic field just on the back side of the lens, namely in the plane I, is denoted by u_1 , which may be evaluated by the diffraction theory of the piston transducer (Appendix A). The illumination function at the converging spherical wave-front surface after the plane acoustic wave traverses through the lens is

$$U_1(\theta) = u_1(\theta)P(\theta)\cos^{1/2}\theta, \tag{6}$$

where θ is the incident angle of the acoustic wave. $P(\theta)$ is the generalized pupil function of the lens for waves traveling in this direction, which describes the complex amplitude of the sound wave transmitted through the lens (see, for example, Born and Wolf, 1972; Wickramasinghe, 1979, and Appendix A). The $\cos^{1/2}\theta$ term is introduced by considering the acoustic imaging system as an aplanatic system for completeness (Richards and Wolf, 1959); it cancels out later. This expression of the illumination function was derived without the assumption of the thin-lens model, i.e., without the paraxial approximation, so the result is valid for any large aperture of the lens. The acoustic wave is then reflected at the focus by an object with a reflectance function $R(\theta)$, and has the amplitude

$$U_2(\theta) = u_1(\theta)P(\theta)R(\theta)\cos^{1/2}\theta. \tag{7}$$

This reflected wave is refracted by the lens again and arrives at the transducer; in this direction the lens pupil function is again $P(\theta)$ (the approximation is made that P is the same in both directions). The acoustic field at the transducer is then

$$U_3(\theta) = P^2(\theta)u_1^2(\theta)R(\theta). \tag{8}$$

The unnormalized signal at the transducer is obtained by summing over the area of the transducer, with radial coordinate r , to give

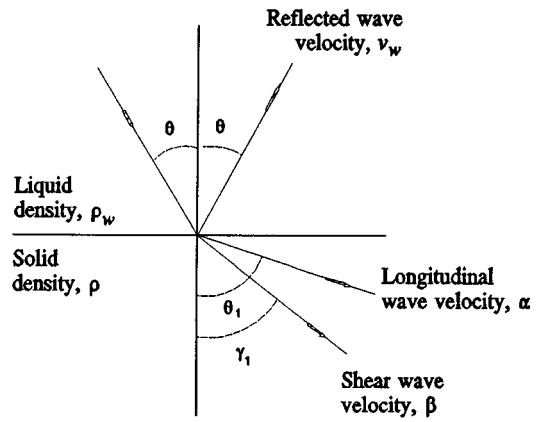


FIG. 11. The reflected and transmitted rays at a liquid-solid interface.

$$V(0) = \int_0^\infty P^2(\theta)u_1^2(\theta)R(\theta)2\pi r dr. \tag{9}$$

Substituting $f \cdot \sin\theta = r$, $f \cdot \cos\theta \cdot d\theta = dr$, where f is the focal length, this may be written

$$V(0) = 2\pi f \int_0^{\theta_m} P^2(\theta)u_1^2(\theta)R(\theta)\sin\theta\cos\theta d\theta, \tag{10}$$

where θ_m is the semiangle of the acoustic lens; outside this given limit $P^2(\theta)u_1^2(\theta)R(\theta)$ should vanish.

If the reflecting surface of the object is now moved towards the lens by a displacement $-z$ from the focus, the phase of the wave incident at a given point on the surface will advance by $k_w \cdot z$, and waves returning to the lens will advance their phase by twice this, so that the normalized signal at the transducer is now (Atalar, 1989; Yu, 1991)

$$V(z) = \int_0^{\theta_m} P^2(\theta)u_1^2(\theta)R(\theta) \times \exp[-i2k_w z \cos\theta] \sin\theta \cos\theta d\theta, \tag{11}$$

where k_w is the wave number of sound in the liquid and z is the defocus.

It is easy to see that for a given lens the functions $P(\theta)$ and $u_1(\theta)$ are known, and the $V(z)$ function is completely determined by the reflectance function $R(\theta)$. In practice, because $R(\theta)$ is a complex function of the elastic properties of the specimen under test, the $V(z)$ function is thus functionally related to the elastic properties of the specimen. Any material changes will alter the $V(z)$ response via $R(\theta)$ changes. Let us therefore discuss the reflectance function in a little more detail.

The reflectance function of materials immersed in liquid has been studied extensively both theoretically and experimentally over the last 50 years (Thomson, 1950; Haskall, 1953; Bertoni and Tamir, 1973; Überall, 1973; Brekhovskikh, 1980; Bogy and Gracewski, 1983). The reflectance function for waves in a liquid incident on the surface of an isotropic nonlayered solid may be derived as follows. The variables are defined with reference to Fig. 11: ν_w and θ are the velocity and angle of incidence of the waves in the liquid, whose density is ρ_w ; α , θ_1 and β , γ_1

are the velocities and angles of refraction of the longitudinal and shear waves in the solid, whose density is ρ . Snell's law relates θ_1 and γ_1 to θ as

$$\frac{\sin \theta}{v_w} = \frac{\sin \theta_1}{\alpha} = \frac{\sin \gamma_1}{\beta}. \quad (12)$$

Impedances are then defined by

$$Z_0 = \frac{\rho_w v_w}{\cos \theta}, \quad Z_L = \frac{\rho \alpha}{\cos \theta_1}, \quad Z_S = \frac{\rho \beta}{\cos \gamma_1}, \quad (13)$$

$$Z_{\text{tot}} = Z_L \cos^2 2\gamma_1 + Z_S \sin^2 2\gamma_1. \quad (14)$$

Then the reflectance function is

$$R(\theta) = (Z_{\text{tot}} - Z_0) / (Z_{\text{tot}} + Z_0). \quad (15)$$

A typical example of $R(\theta)$ for a water-aluminum half-space is shown in Fig. 12(a) illustrating some features of $R(\theta)$. R is a complex function, so in Fig. 12(a) the modulus of R (solid line) is referred to the left ordinate and the phase of R (dashed line) to the right ordinate. The modulus of R is characterized by four features: (1) the value for zero angle of incidence $\theta=0$; (2) the cusp near $\theta=13.59^\circ$ where $|R|$ first rises to one, which corresponds to the longitudinal-wave critical angle of aluminum; (3) the kink near $\theta=28.52^\circ$ where the value of $|R|$ next rises to one, which corresponds to the shear-wave critical angle for aluminum; and (4) the slight dip near $\theta=30.57^\circ$ just past the kink, which corresponds to the Rayleigh-wave critical angle for water-aluminum. Note that above the shear-wave critical angle no energy can be propagated into the solid, so $|R|$ beyond the shear-wave critical angle must be unity. The slight dip that occurs at the Rayleigh-wave critical angle is due to the use of a little trick in our evaluation of $|R|$, that is, we have evaluated $|R|$ along the $\theta' = \theta - i0.0001$, rather than along the θ real axis. By use of this trick it is possible to provide information about the existence of the leaky Rayleigh wave from only an $|R|$ curve. The phase of R , normalized by 2π in the figure, also experiences small fluctuations around the longitudinal critical angle, but its most dramatic behavior occurs near and at the Rayleigh-wave critical angle $\theta_R = 30.57^\circ$, and as can be seen the phase changes by almost 2π over a fairly small change in the incidence angle. This phase transition indicates the existence of nonspecular reflection.

The $V(z)$ curve for this example, which was based on Eq. (11) at $f=1.7$ GHz, is illustrated in Fig. 12(b), from which one can see that a series of regular periodical oscillations occurs on the negative z side. The phase transition in the $R(\theta)$ curve shown in Fig. 12(a) is responsible for these oscillations in the $V(z)$ curve. Because the dominant feature in the $V(z)$ curve is the behavior of the reflectance function around the Rayleigh angle, it is essential for obtaining a good acoustic material signature to use a lens of numerical aperture large enough to include the Rayleigh angle.

In summary, the Fourier theory and the ray model offer two different insights into imaging theory. Both enable $V(z)$ to be calculated *ab initio*. From the point of view of mathematical treatment, the former is a complete integral solution of the problem, and the latter is only the discretized solution of the same problem. The advantage of integral analysis is that one does not need to know about Rayleigh-wave modes,

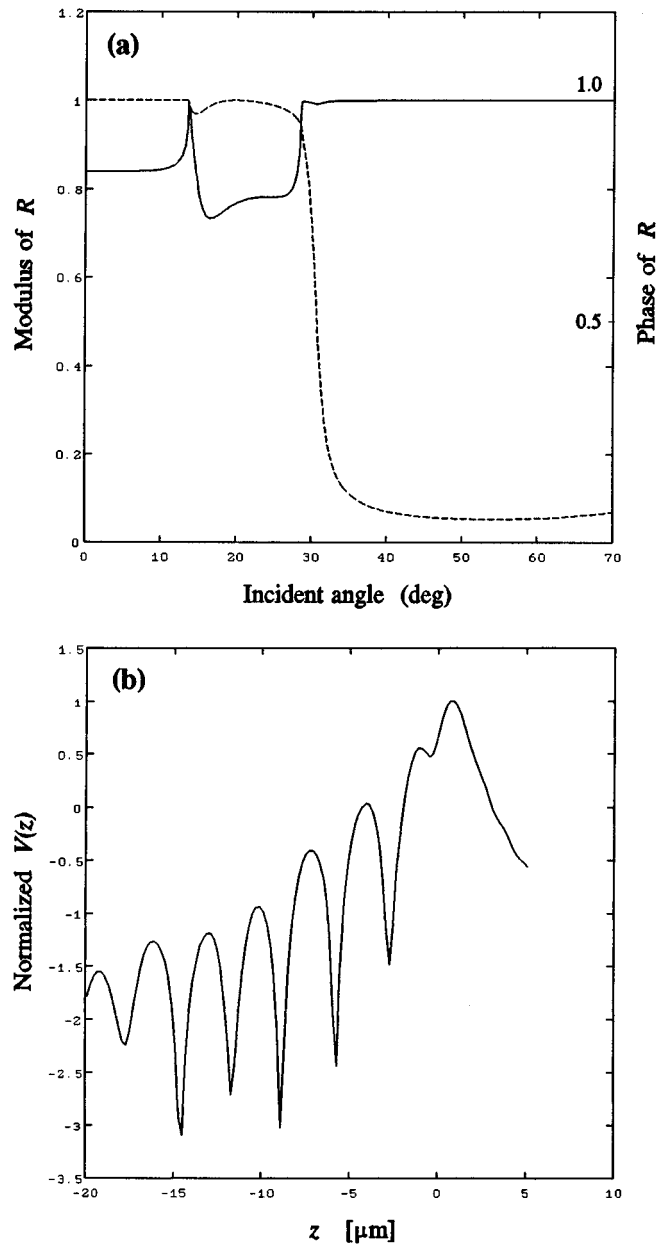


FIG. 12. (a) $R(\theta)$ vs incident angle θ for water-aluminum half-space: solid line, modulus of R ; dashed line, phase of R normalized by 2π ; (b) $V(z)$ curve for the same sample.

nor does one need to calculate the critical angles explicitly; the effect of all rays incident at the critical and noncritical angles are automatically taken into account when the entire converging beam is analyzed by the stationary-phase method in the integral. The discretization treatment must first determine the critical angles before $V(z)$ can be calculated. This is a difficult task, especially for layered structures, because the guided waves in them are dispersive, so that these critical angles are frequency dependent (see Sec. V). However, because integral evaluations are carried out numerically, one cannot easily see with this approach how the various geometric and acoustic parameters of the lens and object influence $V(z)$. On the other hand, the ray optics discretization treatment makes it relatively easy to see how these parameters influence $V(z)$. The main advantage of the ray optics ap-

proach is that it can clearly provide a useful physical explanation of the acoustic material signature and may be used to develop new fields of application for the $V(z)$ effect. Both methods are thus of importance for interpreting the contrast quantitatively.

IV. ELASTIC MICROANALYSIS BY $V(z)$ MEASUREMENT

Having described the general principles of the acoustic microscope and of $V(z)$ theory, we can now consider the application of the $V(z)$ function to characterization of solid materials. The $V(z)$ effect has played a very important role in both acoustic imaging and quantitative measurement in the nondestructive testing of materials. As regards acoustic imaging measurements, the $V(z)$ curves have been effectively employed, for example, in the interpretation of contrast in acoustic images, and in image signal-processing techniques for obtaining enhanced false-color micrographs (Hammer and Hollis, 1982). A new field of acoustic metrology for measuring elastic properties of materials non-destructively on a microscopic scale has grown out of the quantitative measurements. Here we present only examples of successful applications of quantitative measurements, that is, of experimental elastic microanalysis by measuring $V(z)$.

A. Examination of the reflectance function

The amplitude and phase of $V(z)$ can be inverted to deduce the full reflectance function $R(\theta)$ in amplitude and phase (Liang, Kino, and Khuri-Yakub, 1985). To demonstrate this, by use of a suitable change of variables

$$u \equiv k_w z, \quad t \equiv \frac{1}{\pi} \cos \theta,$$

Eq. (11) may be rewritten as

$$V(u) = \int_{1/\pi}^{\cos \theta_m / \pi} P^2(t) u_1^2(t) R(t) \exp[-i2\pi u t] t dt. \quad (16)$$

This can be recognized as a Fourier transform, with $V(u)$ and $\{P^2(t)u_1^2(t)R(t)t\}$ as the transform pair. Of course, the limits of the integration in Eq. (16) should be from $-\infty$ to $+\infty$, but since $\{P^2(t)u_1^2(t)R(t)t\}$ vanishes outside the given limits, this makes no difference. The Fourier transform may be inverted to yield

$$R(t) = \frac{1}{P^2(t)u_1^2(t)t} F^{-1}[V(u)]. \quad (17)$$

Thus, by measuring $V(u)$ and inverse-Fourier-transforming it, one may estimate the reflectance function. In order to deduce $R(\theta)$ from a simple inversion of $V(z)$, it is necessary to measure it as a complex-valued function, i.e., with both amplitude and phase information. This can be done by using an accurate amplitude and phase measurement system (Liang, Bennett, *et al.*, 1985). However, in most conventional commercial acoustic microscopes the video signal is measured after detection by an envelope detector, so that the phase information is lost. In this case it is necessary to employ a phase retrieval algorithm (Fright *et al.*, 1989) to reconstruct phase information from a modulus only $V(z)$.

B. Measurement of phase velocity of surface acoustic waves

Material characterization can be carried out by measuring the propagation characteristics, that is, the phase velocity and attenuation, of a leaky Rayleigh wave excited in the sample. The periodicity and decay of oscillations in $V(z)$ directly relate to these properties. The phase velocity is simply determined from the interval Δz in the $V(z)$ curve [see Eq. (5)]. For a conventional commercial SAM, for example, the Leica ELSAM, which employs water as a coupling material and a semiangle of 50° at 1.3–2.0 GHz, allowing a z -scan distance of $20 \mu\text{m}$, the measurement of the phase velocity can be carried out effectively from about 2000 m/s up to 6000 m/s. Other coupling liquids might make the $V(z)$ curve measurements more effective for materials with both higher and lower velocities than water. The relative accuracy of the velocity measurement can easily be about 1 percent (Yu and Boseck, 1994). A best measured accuracy of 0.2 percent was reported by use of the line-focus-beam SAM (Kushibiki and Chubachi, 1985). In addition to measuring the velocity of Rayleigh waves, Quate (1980) has pointed out that it should be possible to use the $V(z)$ response to record the longitudinal velocity in an object on a microscopic scale. The basic approach is to choose the coupling liquid so that the lens angular aperture only includes the longitudinal critical angle. In this case, the $V(z)$ null spacing Δz can be related to the longitudinal velocity α in the solid [using Eq. (5) with α replacing ν_R]. Moreover, in a small number of materials of intermediate elastic stiffness (mainly polymers of relatively high moduli such as PMMA), lateral longitudinal waves can take the place of Rayleigh waves. These waves, also known as surface-skimming compressional waves, propagate parallel to the liquid-solid interface when the angle of refraction is 90° (Tamir, 1972), so that the longitudinal critical angle replaces the Rayleigh angle in calculating the period of the oscillations in the $V(z)$ curve. Then, the phase velocity of a surface-skimming compressional wave can be determined from $V(z)$. In any measurement of the phase velocity, Fourier analysis usually is used on the $V(z)$ curve for analyzing its period of oscillation in order to obtain sufficient measurement accuracy.

C. Measurement of attenuation of surface acoustic waves

The attenuation coefficient of surface acoustic waves on a liquid-loaded specimen is characteristic of bulk elastic properties, as well as topographic variations of the surface. The grain size, porosity, density of micro cracks, and so on, near the surface of materials can all influence the measured values. Thus SAW attenuation is a sensitive indicator of surface characterization.

If there is a loss in the specimen, the velocities α and β of the longitudinal wave and shear wave in the specimen become complex descriptions α^* and β^* , and can be expressed as

$$\begin{aligned} \alpha^* &= \alpha / (1 + iL_\alpha / 2\pi), \\ \beta^* &= \beta / (1 + iL_\beta / 2\pi), \end{aligned} \quad (18)$$

where L_α and L_β are the attenuation factors of the longitudinal wave and shear wave in the specimen per wavelength in decibels. The complex wave numbers are

$$k_\alpha^* = \frac{\omega}{\alpha^*} = \frac{\omega}{\alpha} (1 + iL_\alpha/2\pi) = \frac{\omega}{\alpha} + i \frac{L_\alpha}{\lambda_\alpha},$$

$$k_\beta^* = \frac{\omega}{\beta} + i \frac{L_\beta}{\lambda_\beta}, \quad (19)$$

where ω is the circular frequency, and λ_α and λ_β are the wavelengths of the longitudinal and shear waves in the specimen, respectively. With this complex wave-number description, the reflectance function $R(\theta)$ of a plane acoustic wave at a liquid-specimen interface is again evaluated by Eq. (15). The $V(z)$ curve can also be calculated by use of Eq. (11). Usually, attenuation reduces the amplitude of the reflectance function close to and around the Rayleigh angle, hence reducing the depth of dips ΔV in the $V(z)$ curve, but with the interval between dips unvaried. An example of the effects of attenuation on $|R(\theta)|$ and $V(z)$ is shown in Fig. 13, in which the solid lines indicate the nonattenuation cases while the dashed lines indicate the attenuation cases, respectively.

Using a SAM, one may carry out an attenuation measurement in various ways, for example, fitting the parameters to the $V(z)$ curve (Yamanaka, 1982) and direct measurement with use of an annular lens (Smith and Wickramasinghe, 1982). The parameter-fitting method uses an exact theoretical model of $V(z)$ to simulate the measured $V(z)$ curve. SAW attenuation is introduced into the model in order to match the measured data more accurately by allowing the elastic constants to be complex [Eqs. (18) and (19)]. A value for the attenuation can then be found by forward optimization of the measured $V(z)$ curve. With the annular lens method, that is, with an absorbent or reflective aperture stop in the center of the lens as shown in Fig. 14, the purely longitudinal specular reflection beam (the wave path A in Fig. 14) is not detected by the transducer. Only the nonspecular reflection (the longitudinal/SAW/longitudinal wave path B) enters the lens and gives rise to the output signal, and so the $V(z)$ curve is free from interference. The lens output simply records an exponential decay of the signal. The gradient of the $V(z)$ curve reveals the SAW attenuation coefficient in the specimen.

D. Determination of elastic constants of bulk materials

Elastic constants of bulk materials (elastic stiffness constants C_{ij}) are basic physical parameters. Their accurate determination has been required for many industrial and science applications. For determination of elastic constants, it is conventional to make velocity measurements of both longitudinal and shear waves by various kinds of ultrasonic methods including the optical diffraction method. The ultrasonic transducers, made of piezoelectric plates at lower frequencies or ZnO thin films at higher frequencies, must usually be fabricated on one end of the specimens, of which both end surfaces are polished with parallelism. Now, because acoustic microscopy utilizes elastic wave illumination, the obtained image relates directly to elastic properties on a mi-

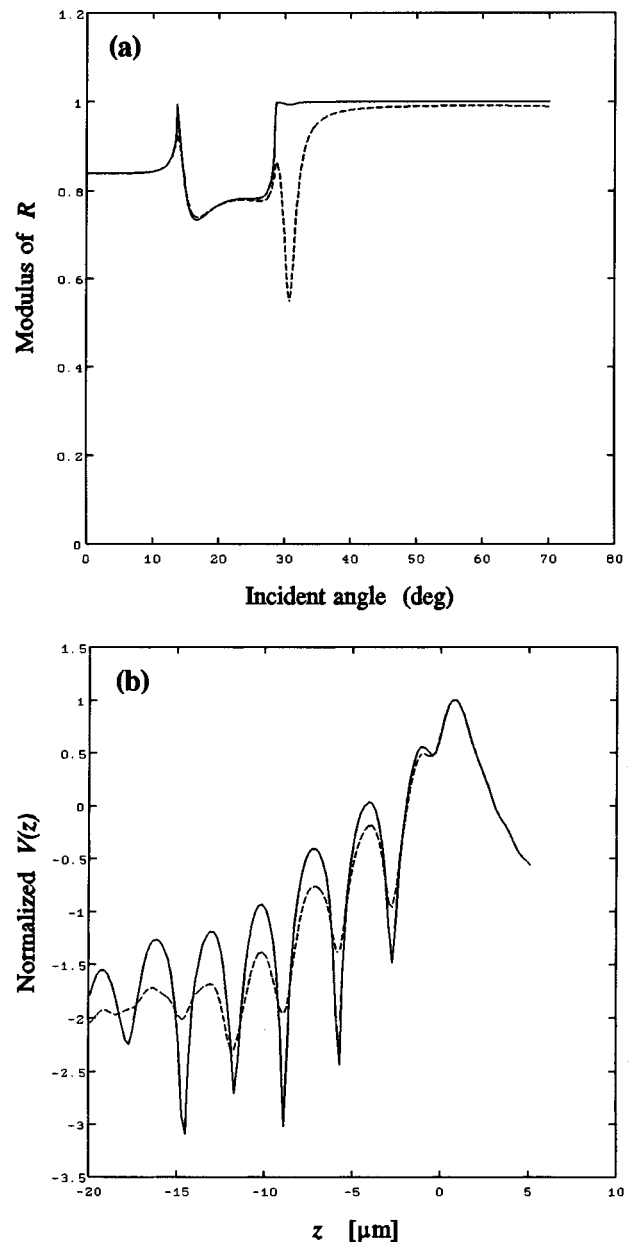


FIG. 13. (a) $|R(\theta)|$ versus incident angle θ for water-aluminum half-space: solid line, nonattenuation case; dashed line, attenuation case; (b) $V(z)$ curves for the same sample: solid line, nonattenuation case; dashed line, attenuation case.

croscopically. Thus, using acoustic microscopy, a new method of measuring the elastic constants of bulk solid materials has been developed. This technique has the great advantage that nondestructive and noncontacting measurements can be made without fabrication of any ultrasonic transducers. The acoustic microscope can precisely measure the velocity of leaky SAWs propagating on the liquid-loaded specimen. The leaky-SAW velocity is directly related to the elastic properties of the specimen, so that it is possible to determine the elastic constants by theoretical analysis. The approach is based on computer fitting the experimental SAW velocity (Kushibiki *et al.*, 1987) and/or on the inversion procedure (Yu and Boseck, 1991). When one seeks a least-squares fit of the SAW velocities between the measured and the calculated

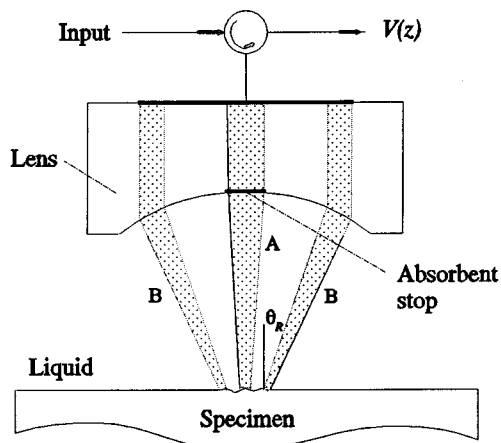


FIG. 14. Schematic geometry of an annular lens.

values, an inversion of the SAW data yields the unknown elastic constants of the specimen.

V. MATERIAL CHARACTERIZATION OF A LAYERED SOLID BY ACOUSTIC MICROSCOPY

Today there are many industrial products and processes that employ structures containing a single thin layer or several thin layers deposited on, or somehow otherwise adhering to, a substrate. Characterizing near-surface properties of such structures, detecting defects below the surface, determining the layer thicknesses, and evaluating the uniformity of the bond are important problems. The scanning acoustic microscope is very suitable for subsurface imaging and nondestructive evaluation of these properties. Since surface waves extend about a wavelength below the surface, even in the reflection model it may be possible to image features that lie below an opaque surface layer and to measure their properties quantitatively on a microscopic scale. Acoustic microscopy offers obvious advantages over conventional microscopy. The propagation properties of SAWs in layered structure are more complicated than in nonlayered structure. In addition to Rayleigh surface waves, other surface wave modes, such as Love wave modes, and Sezewa wave modes (generalized Lamb waves) can be excited in a layered solid. All such surface waves take part in the interference phenomena recorded by a SAM. To understand their dispersion properties and effect on the $V(z)$ function, it is necessary to know something about the propagation characteristics of surface acoustic waves in a layered solid.

A. Dispersion of surface acoustic waves in a layered solid

A thin layer of finite thickness deposited on an isotropic substrate can be used to guide elastic surface waves in the substrate. Introduction of such a layer on top of a free surface of infinite extent provides a characteristic geometric dimension to the propagation medium, and waves may propagate in many different independent modes, all confined to the surface region. Some of these modes are perturbations of the free-surface Rayleigh waves, but others are quite different in character. All such surface waves become dispersive because

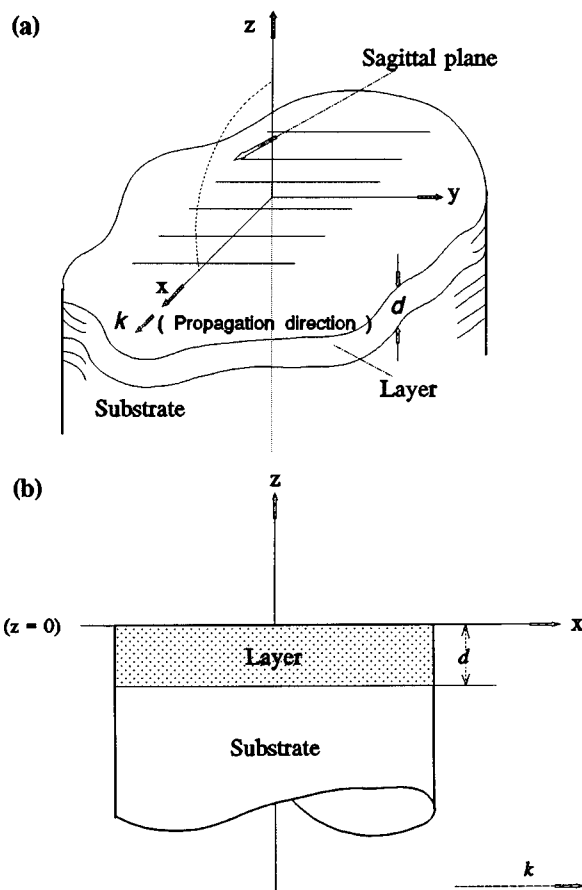


FIG. 15. (a) Coordinate system for wave propagation in thin layer, propagation direction and sagittal plane; (b) geometry of a layered solid in the sagittal plane.

the SAW velocity is now a function of both frequency and the layer thickness and elastic parameters. The coordinate system for the thin-layer problem is illustrated in Fig. 15. The layers of concern are thin, usually of a thickness d less than the wavelength of the surface wave being studied. The waves of interest here will be “straight crested” in the sense that there are no variations of any of the displacement components in a direction parallel to the free surface and perpendicular to the direction of propagation. Thus the disturbance has constant phase and amplitude for each component measured along any line parallel to the y axis.

For the thin-layer/substrate configuration without a liquid contact, detailed reviews of elastic-wave propagation have been presented by Tiersten (1969) and by Farnell and Adler (1972). The effect of the liquid contact has been discussed by Chimenti *et al.* (1982). In the standard analytical approach, waveguide modes in the layer are combined with waves of exponentially decaying magnitude in the solid and liquid half-space. Consider the geometry of Fig. 15. Here the displacement solution in a perfectly elastic, homogeneous, nonpiezoelectric, but anisotropic medium is assumed to be a linear combination of terms of the form (Farnell and Adler, 1972)

$$u_i = U_i \exp[-ikl_3z] \exp[ik(l_1x + l_2y - \nu_R t)] , \quad (20)$$

where U_i is the relative amplitude of the different compo-

nents of each partial wave, k is the wave number, l_1, l_2 , and l_3 are the direction cosines, and ν_R is the SAW phase velocity. If the direction of wave propagation in the surface is taken as x direction, then $l_1 = 1$ and $l_2 = 0$, respectively. Such terms must simultaneously satisfy the equation of motion and the boundary conditions.

Substitution of Eq. (20) into the displacement equations of motion gives the following relation between ν_R, l_3 , and U_i for each medium being considered:

$$\begin{bmatrix} \Gamma_{11} - \rho \nu_R^2 & \Gamma_{12} & \Gamma_{13} \\ \Gamma_{12} & \Gamma_{22} - \rho \nu_R^2 & \Gamma_{23} \\ \Gamma_{13} & \Gamma_{23} & \Gamma_{33} - \rho \nu_R^2 \end{bmatrix} \begin{bmatrix} U_1 \\ U_2 \\ U_3 \end{bmatrix} = \begin{bmatrix} 0 \\ 0 \\ 0 \end{bmatrix} \quad (21)$$

In order to have nontrivial solutions, the determinant of the square matrix in Eq. (21) must be set equal to zero, which produces the secular equation for each medium

$$|\Gamma_{jk} - \delta_{jk} \rho \nu^2| = 0 \quad (j, k = 1, 2, 3) \quad (22)$$

In an isotropic solid the only nonzero terms in the stiffness matrix are $C_{11} = C_{22} = C_{33}$, $C_{12} = C_{13} = C_{23}$, and $C_{44} = C_{55} = C_{66} = (C_{11} - C_{12})/2$, with the result that the relevant algebraic form of the equation of motion, i.e., Eq. (21), now becomes

$$\begin{bmatrix} \Gamma_{11} - \rho \nu_R^2 & 0 & \Gamma_{13} \\ 0 & \Gamma_{22} - \rho \nu_R^2 & 0 \\ \Gamma_{13} & 0 & \Gamma_{33} - \rho \nu_R^2 \end{bmatrix} \begin{bmatrix} U_1 \\ U_2 \\ U_3 \end{bmatrix} = \begin{bmatrix} 0 \\ 0 \\ 0 \end{bmatrix} \quad (23)$$

where ρ is the density of the medium, and

$$\begin{aligned} \Gamma_{11} &= C_{11} + C_{44}l_3^2, & \Gamma_{13} &= (C_{11} - C_{44})l_3, \\ \Gamma_{22} &= C_{44}(1 + l_3^2), & \Gamma_{33} &= C_{11}l_3^2 + C_{44}. \end{aligned} \quad (24)$$

The traction-free boundary condition at the free surface of the layer and the continuity of traction and displacement at the interface between the layer and the substrate then yield one set of homogeneous equations for the constants appearing in the wave solutions in the layer and the liquid and solid half-space (Farnell and Adler, 1972). In order to have nontrivial solutions for this set of homogeneous equations, one must ensure that the ‘‘boundary-condition determinant’’ vanish. This yields a dispersion relation, which relates the phase velocity ν_R of the surface wave to a frequency f , or a product of the frequency and the thickness of the layer, fd , with a unit of $\text{GHz} \cdot \mu\text{m}$. For a given value of fd there is an infinite number of complex-valued solutions for ν_R . The solutions whose real parts are not zero represent propagating wave modes. The modes of a surface-wave solution can be separated into two independent sets: the ‘‘Love modes’’ (Love, 1911) and the ‘‘Rayleigh-like modes.’’ Love modes are waves possessing one displacement component, parallel to the surface and perpendicular to the direction of propagation (transverse displacements). Rayleigh-like modes are waves with sagittal-plane displacements (in the direction of propagation and normal to the surface). The sagittal-plane displacements (Rayleigh-like waves) and transverse displacements (Love waves) are completely uncoupled. Both

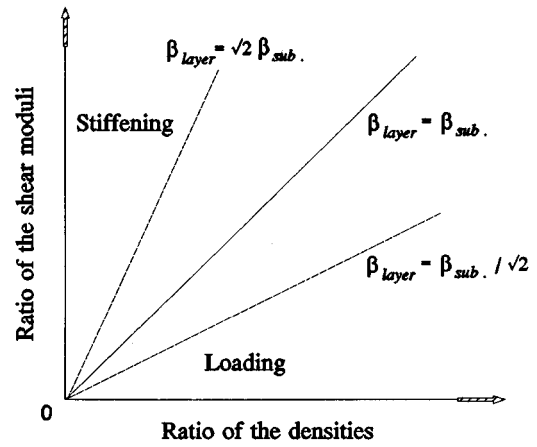


FIG. 16. Sufficient conditions for stiffening and loading for isotropic material combinations.

types of wave are dispersive in that the phase velocity now depends on the frequency of excitation, and they have an unlimited number of higher-order modes for any given combination of materials.

It is possible further to characterize the propagation properties of these modes by the relative values of the shear bulk wave velocity of the layer (β_{layer}) and the substrate ($\beta_{substrate}$) involved. The propagation properties for Rayleigh-like waves can be separated into three distinct categories, shown in Fig. 16, where the ordinate is the ratio of the shear moduli and the abscissa is the ratio of the densities. For layer-substrate combinations lying above the $\beta_{layer} = \sqrt{2}\beta_{substrate}$ line, i.e.,

$$\beta_{layer} > \sqrt{2}\beta_{substrate},$$

the layer is said to ‘‘stiffen’’ the substrate because the presence of the layer increases the surface-wave velocity above that of the Rayleigh wave in the substrate, whereas for material combination below the $\beta_{layer} = \beta_{substrate}/\sqrt{2}$ line, i.e.,

$$\beta_{layer} < 1/\sqrt{2}\beta_{substrate},$$

the layer is said to ‘‘load’’ the substrate because the velocity of the free-surface Rayleigh mode on the substrate material is decreased by the presence of the layer.

For the stiffening case there exists only a single propagating mode, the Rayleigh-wave mode, whose phase velocity increases monotonically with frequency. Figure 17(a) shows an example of the dispersion curve for the stiffening case, in which a chromium layer stiffens the copper substrate. The dispersion curve has positive slope. At zero frequency the phase velocity equals the Rayleigh-wave velocity in the substrate, and it increases up to the shear-wave velocity of the substrate ($\beta \approx 2330$ m/sec) at a particular value of fd as fd increases. For a larger value than this cutoff value of fd , this mode of propagation does not exist for this layer-substrate combination.

For the loading case, an unlimited number of Rayleigh-like modes and Love modes can exist, depending on the layer-substrate combinations and fd . The lowest mode of the Rayleigh-like modes is generally considered to be a modification of the Rayleigh surface wave in the substrate and again is simply called the Rayleigh mode; higher modes are

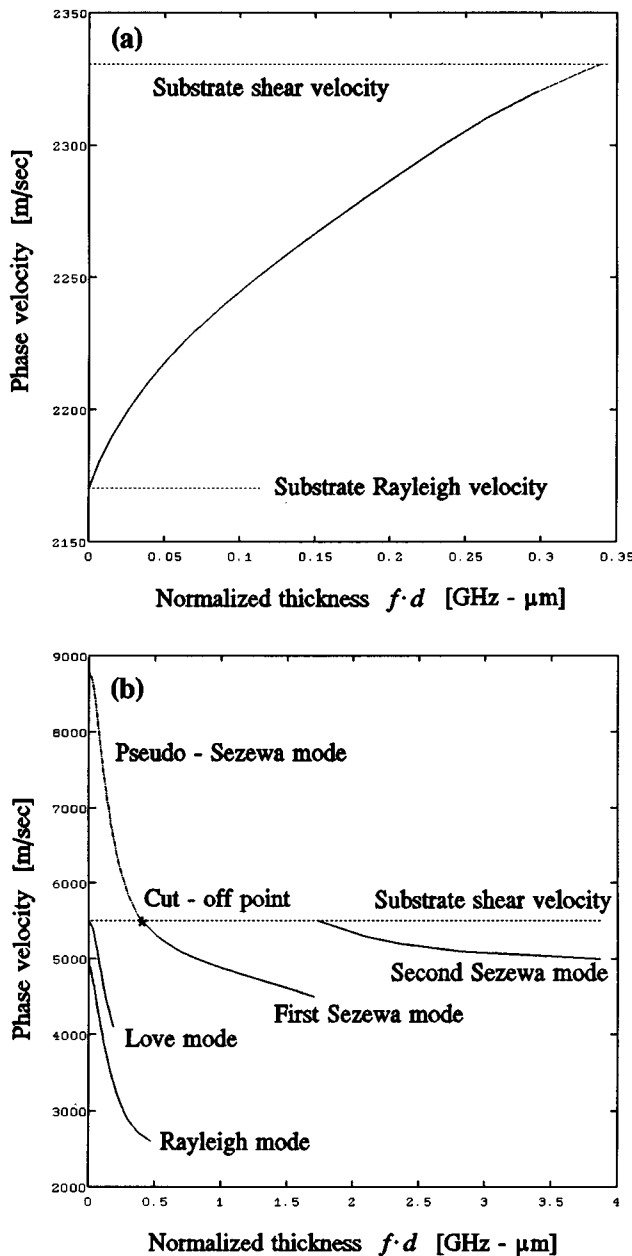


FIG. 17. Dispersion curves in layered materials: (a) chromium on copper ($\beta_{\text{layer}} > \beta_{\text{substrate}}$), the layer stiffens the substrate; (b) tungsten on silicon ($\beta_{\text{layer}} < \beta_{\text{substrate}}$), the layer loads the substrate.

called Sezewa modes after their discoverer Sezewa (Sezewa and Kanai, 1935). For the lowest mode, i.e., the Rayleigh mode, the dispersion curve starts with a negative slope at the Rayleigh velocity of the substrate, and as the frequency increases the velocity monotonically decreases to asymptotically approach the Rayleigh velocity appropriate to a free surface of the layer material. Sezewa modes require a minimum layer thickness to propagate for a given frequency, or conversely, for a given layer thickness there is a cutoff frequency below which the mode cannot propagate unattenuated. Therefore each Sezewa mode may be considered to consist of two parts: the Sezewa mode and the pseudo-Sezewa mode. The Sezewa mode has a low-frequency cutoff

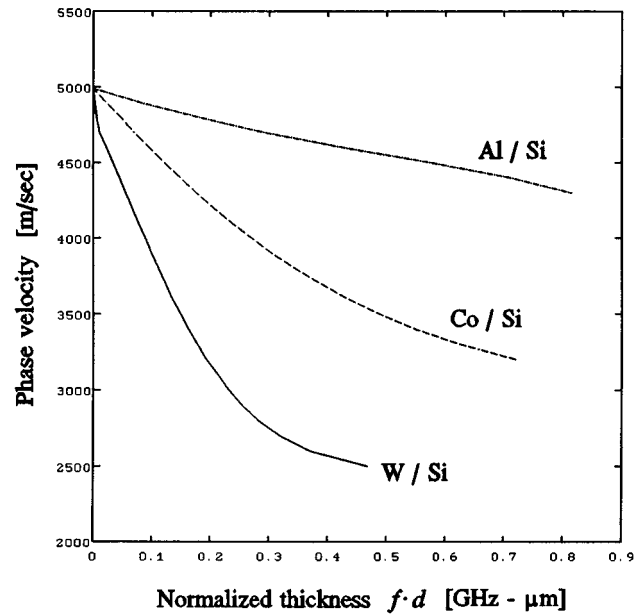


FIG. 18. Dispersion curves of the Rayleigh wave: dash-dotted line, Al/Si; dashed line, Co/Si; solid line, W/Si.

at which the phase velocity is equal to the shear velocity of the substrate material and has a high-frequency asymptote equal to the layer shear velocity, in contrast to the first Rayleigh mode, which has an asymptote equal to the Rayleigh velocity of the layer material. The pseudo-Sezewa mode exists at low frequencies. At zero frequency its velocity equals the velocity of a surface-skimming longitudinal wave (Tamir, 1972) at the substrate. The velocity decreases to that of the shear wave of the substrate material at the cutoff frequency. The pseudo-Sezewa mode radiates acoustic energy into the substrate. Figure 17(b) shows the dispersion curves for the loading case, all of which have negative slope. The material combination is a tungsten layer on a silicon substrate. The calculation of the dispersion curves follows Tiersten (1969) by evaluation of a fourth-order dispersion equation. This figure shows the phase velocity curves for the three Rayleigh-like modes, namely, the lowest Rayleigh mode and the first and second Sezewa modes. As mentioned above, as fd increases, the phase velocity of the lowest Rayleigh mode decreases asymptotically to the Rayleigh-wave velocity of the tungsten layer ($v_R \approx 2668$ m/sec), whereas the phase velocity curve of the Sezewa wave mode decreases asymptotically to the shear-wave velocity of the tungsten layer ($\beta \approx 2880$ m/sec). The first Sezewa wave has a cutoff wave number of $fd = 0.394$ GHz $\cdot\mu\text{m}$, at which the phase velocity is equal to the shear-wave velocity in the substrate silicon ($\beta \approx 5500$ m/sec), and the leaky pseudo-Sezewa mode and the leaky Sezewa mode are distinguished at this cutoff point.

In Fig. 18 the dispersion curves are shown for the three particular layer/substrate material combinations, i.e., an aluminum layer on a silicon substrate (dot-dashed), a cobalt layer on a silicon substrate (dashed line), and a tungsten layer on a silicon substrate (solid line). The dispersion curves are presented only for the lowest Rayleigh-wave modes. This figure shows that the dispersion curves clearly depend on the material properties of the layered structures. The dispersion

curve for the W/Si combination indicates a larger negative gradient. A small variation of fd causes a larger velocity difference, whereas, the dispersion curve for the Al/Si combination shows a flat characteristic in a quite large region of fd . This indicates that a large variation in the thickness of the Al layer causes only a slight decrease in the phase velocity of the leaky SAW. This study of the characteristics of the dispersion curve is of great significance in analyzing the resolution of layer-thickness measurements by a SAM.

Love modes exist only if the layer has a shear-wave velocity lower than that of the substrate. The velocity of the first of these Love modes becomes equal to the shear velocity of the substrate material when the layer thickness vanishes. At high frequencies, the velocity of this mode becomes asymptotic to the shear velocity of the layer material. An example of the first Love mode is also shown in Fig. 17(b). The higher Love modes all have low-frequency cutoffs when the phase velocity becomes equal to the shear velocity of the substrate material, and at high frequencies the phase velocities of each mode approach asymptotically the shear velocity of the layer material.

If the shear velocity of the layer lies between $\sqrt{2}$ and $1/\sqrt{2}$ times that of the substrate, the situation is more complicated, and it involves the ‘‘Stoneley’’ modes for the two materials. In this paper only the Rayleigh-like modes are of interest.

B. Behavior of $V(z)$ for a layered structure

When a conventional SAM equipped with a spherical lens is used to image a layered structure, many possible surface acoustic wave modes are excited in the specimen, because all incidence angles are found at the object interface. In this case, the $V(z)$ function can also be calculated by the Fourier optics approach, i.e., Eq. (11). However, the physical model of $V(z)$ for layered structures must be further extended.

1. Multiple-ray interference model of $V(z)$

The double-ray model of $V(z)$ described above works for smooth nonlayered isotropic solids, in which only one leaky surface wave is excited. In a layered structure, more than one leaky surface wave may be excited within the half aperture of the SAM lens. All acoustic rays incident on the specimen at the leaky-SAW critical angle may contribute to $V(z)$ after undergoing nonspecular reflection. The combined effect of all these leaky wave modes determines the nature of the acoustic material signature. From the interference point of view, a multiple-ray interference model should be considered.

Figure 19 shows the cross-sectional geometry of an acoustic beam that is used to explain the multiple-ray interference mechanism in the $V(z)$ curve. Each leaky-SAW mode associated with the wave propagating along B_i , $i = 1, 2 \dots n$, is excited at its critical angle by the focused acoustic waves and propagates with its characteristic phase velocity on the boundary. Now, we assume that the construction mechanism for the $V(z)$ curve is a linear system, so that we can take a superpositional model for the total interference output as

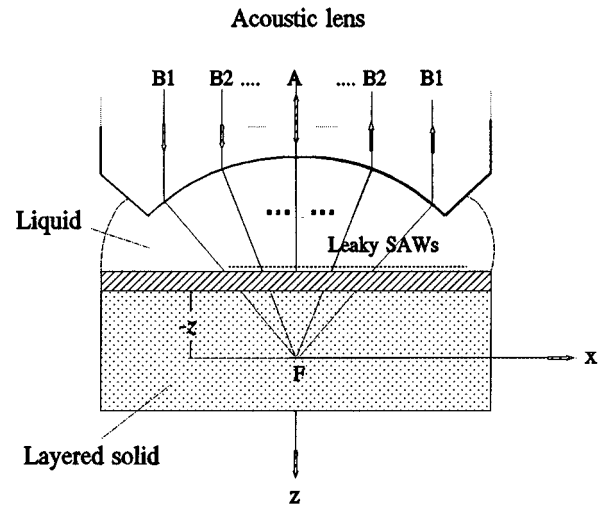


FIG. 19. Multiple-ray interference model of $V(z)$.

$$V(z) = V_L(z) + \sum_{k=1}^n V_T^k(z), \quad (25)$$

where $V_L(z)$ is the transducer output due to the acoustic wave propagating along path A directly reflected from the surface of the sample, and $V_T^k(z)$, $k = 1, 2 \dots n$, are the transducer outputs associated with waves propagating along B1, B2, ..., due to the leaky-SAW components propagating on the boundary. Due to multiple-ray interference, the variation of the $V(z)$ curve is seen to be irregular both in the depth of the minima and in the unequal spacing between minima. It is impossible to determine the phase velocities of leaky SAWs straightforwardly using the simple double-ray formula, Eq. (5). This fact makes it difficult to use an SAM for material characterization of a layered structure through $V(z)$ measurement. The conventional SAM cannot choose and identify single leaky-SAW modes from the obtained $V(z)$ curve. We must carry out an analysis of the oscillation characteristics of the $V(z)$ curve to extract the relevant SAW mode for material characterization. This analysis requires, first, a detailed understanding of the propagation characteristics of a leaky SAW in a layered solid, and then wave-form analyses and parameter studies of the $V(z)$ curve in association with a study of the propagation characteristics of the leaky-SAW mode.

2. Wave-form analysis of the $V(z)$ curve

Here, we shall describe the behavior of $V(z)$ in layered structures. The use of these results for understanding the effect of various leaky-SAW modes on the $V(z)$ curve, and the identification of these leaky-SAW modes which are most likely to produce the oscillations of the relevant $V(z)$ curve, is of primary interest.

To calculate $V(z)$ in a layered solid following the Fourier optics approach, Eq. (11), we must first evaluate the reflectance function of the plane acoustic waves that are incident on the layered solid. Usually, the reflectance function R for a layered solid immersed in liquid, for example water, can be formally written as (Kundu *et al.*, 1985; Yu, 1991, and Appendix B)

$$R(\xi) = \frac{N(\xi)}{D(\xi)} = \frac{\eta_w(J_{11}J_{22} - J_{12}J_{21}) + i\rho_w v_w^2 \kappa_w^2 (J_{11}J_{23} - J_{21}J_{13})}{\eta_w(J_{11}J_{22} - J_{12}J_{21}) - i\rho_w v_w^2 \kappa_w^2 (J_{11}J_{23} - J_{21}J_{13})}, \quad (26)$$

where $\xi = k_w \sin \theta$, k_w is the wave number of sound in the liquid, θ is the incidence angle, ρ_w is the density of the liquid, v_w is the longitudinal velocity in the liquid, and J is the chain product of Thomson-Haskell layer matrices (Thomson, 1950; Haskell, 1953).

Figure 20 presents an example of a reflectance function for a copper substrate with a silver layer. The understanding of the excitation of leaky-SAW modes from the reflection curves is of primary interest. Because the layer material has a lower shear velocity than that of the substrate, this is a single-layer “loading” case. For a fixed set of materials, the reflectance function R is a function of the incidence angle θ and fd . In Fig. 20(a), $|R|$ vs θ curves are presented for different values of fd . The curves for $fd > 0$ have been shifted downward for clarity and ease of comparison. In the top curve, $d = 0$ and the reflection function shows the $|R|$ curve for a water-copper half-space. As mentioned above, in this nonlayered case there is only a single SAW mode, i.e., a Rayleigh mode can be excited. The slight dip in the right-hand portion of the curve at the Rayleigh-wave critical angle indicates the excitation of this SAW mode (see Sec. III.B.3). As the thickness increases, the other curves in Fig. 20(a) indicate, by additional slight dips, that several surface-wave modes are excited depending on fd . This can be seen more clearly in the modulus and phase curves of R for the case $fd = 4.0$ in Fig. 20(b). There are three small dips in the right-hand portion of the $|R|$ curve, where three corresponding phase transitions by almost 2π over a small change of θ in the phase curve occur. These phase transitions arise from various leaky-SAW modes excited in the layered solid.

Equation (26) for the reflectance function contains, as a by-product, the characteristic equation for the propagation of leaky-SAW modes along the liquid-layered solid interface. The vanishing of the denominator in $R(\xi)$, namely, $D(\xi) = 0$, is the characteristic equation for such waves. That is, the propagating SAWs correspond to poles ξ_p of the reflection coefficient. Because of the presence of liquid the pole ξ_p becomes complex and can be expressed as

$$\xi_p = \text{Re}(\xi_p) + i\text{Im}(\xi_p), \quad (27)$$

where Re and Im refer to real and imaginary parts, respectively. From Eq. (27) we obtain the phase velocity v_R of the leaky SAW and the Schoch displacement parameter Δ_s (see Fig. 8)

$$v_R = \omega / \text{Re}(\xi_p), \quad \Delta_s = 2 / \text{Im}(\xi_p), \quad (28)$$

where ω is the circular frequency.

This brings us to the features of $V(z)$ for a layered structure. In Fig. 21, we first present an example of a $V(z)$ curve for glass (solid line) and glass with a chromium layer of $0.1 \mu\text{m}$ thickness. The calculations of $V(z)$ curves were carried out at $f = 1.8 \text{ GHz}$. The two $V(z)$ s have different periodicities, which results in their becoming progressively out of

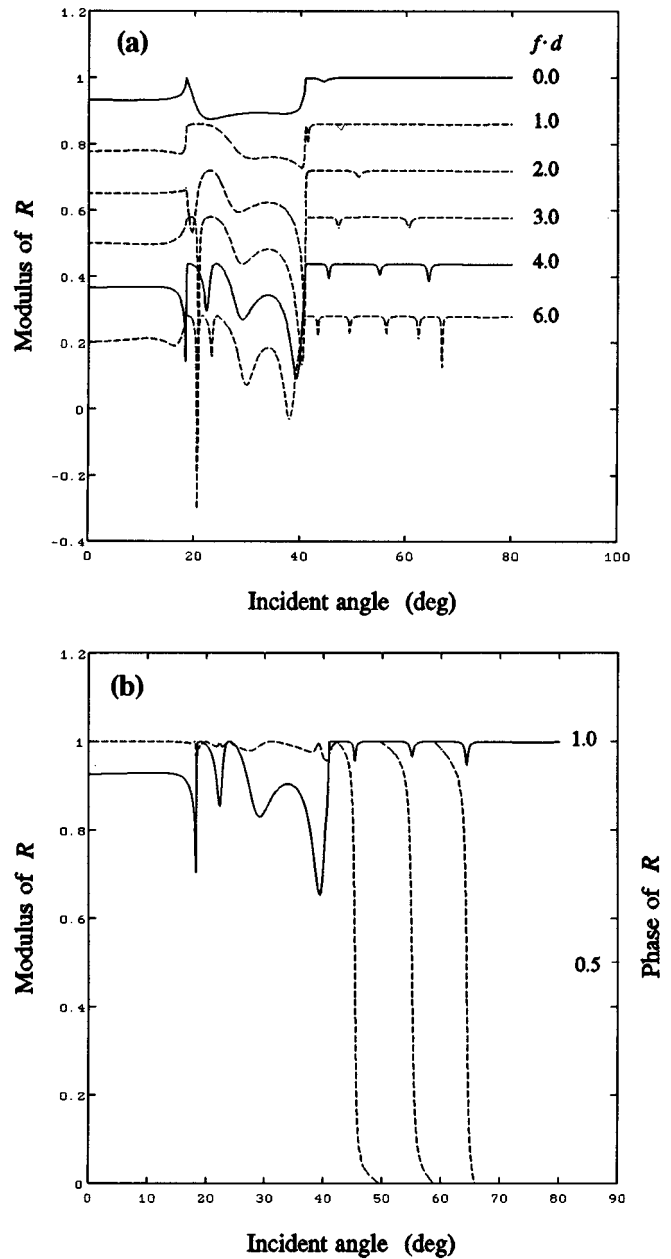


FIG. 20. $R(\theta)$ for Ag/Cu structure immersed in water: (a) $|R|$ vs incident angle θ for various values of fd with a unit of $\text{GHz}\cdot\mu\text{m}$; (b) R vs θ for $fd = 4.0$. Solid line, modulus of R ; dashed line, phase of R normalized by 2π .

phase as the defocus is increased. The difference in the spacing of the dips for the two curves is related to the decrease in the phase velocity of the Rayleigh-wave mode as the layer appears. Marked on this figure are two points at which the contrast is strong; however, the contrast at A will be the reverse of that at B.

Next, we simply carry out wave-form analysis and parametrical studies of the $V(z)$ curve in a layered solid in order to see the effects of various possible leaky-SAW modes on the $V(z)$ curve. The $V(z)$ curve of a layered solid depends on the layer thickness and the material properties of the layer and the substrate, so the situation is quite complicated. The material properties of a thin layer are also generally different

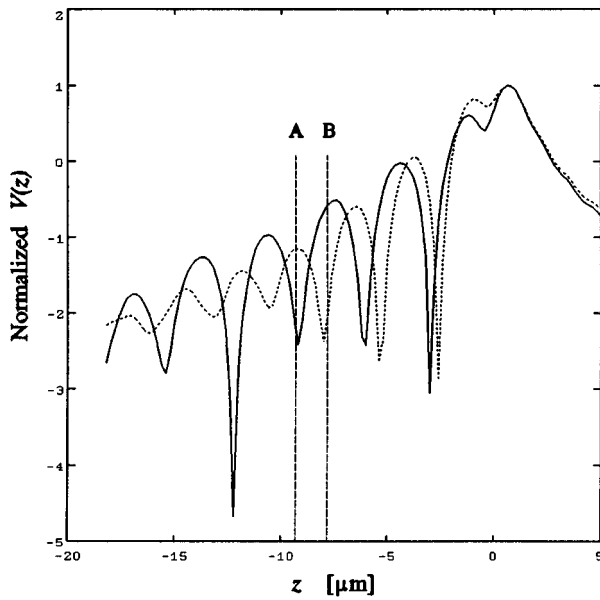


FIG. 21. Illustration of the manner in which $V(z)$ curves differ for materials of differing Rayleigh velocity, and manner in which contrast in a SAM varies with defocus for two elastically dissimilar materials.

from those of a bulk material. Here we take only two particular examples of wave-form analysis of the $V(z)$ curve, using a given layer thickness and given material properties.

Figure 22 shows the $V(z)$ curves for a specimen of a silicon substrate with an aluminum layer, which indicates the effect on $V(z)$ of various layer thicknesses, i.e., various possible SAWs excited in the sample. The parameters of the scanning acoustic microscope in the calculations of these $V(z)$ curves are: semiangle 50° and frequency $f = 1.8$ GHz. In this figure the solid and dashed lines show the results for

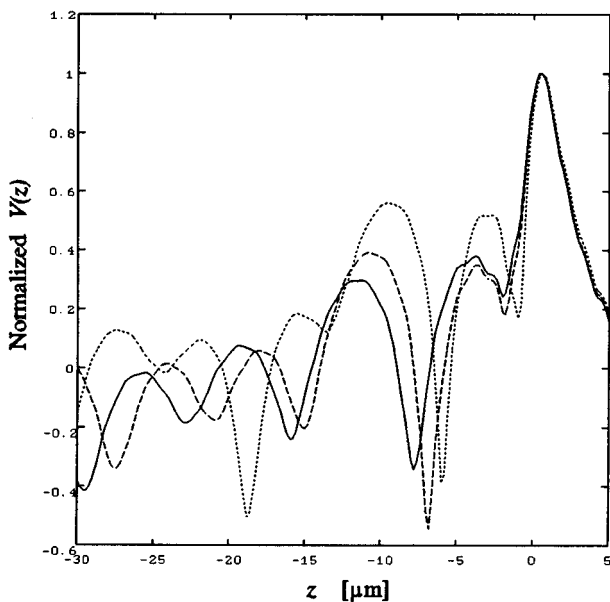


FIG. 22. $V(z)$ curves for Al/Si sample: Solid line, $0.2 \mu\text{m}$; dashed line, $0.4 \mu\text{m}$; dotted line, is $0.6 \mu\text{m}$.

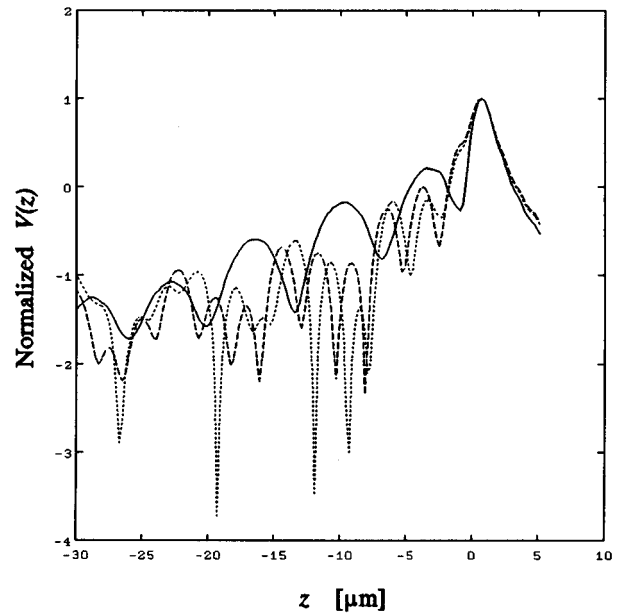


FIG. 23. $V(z)$ curves for Co/Si sample: Solid line, $0.1 \mu\text{m}$; dashed line, $0.8 \mu\text{m}$; dotted line, $2.0 \mu\text{m}$.

Al layers of $0.2 \mu\text{m}$ and $0.4 \mu\text{m}$ thickness, respectively. The oscillations of both $V(z)$ curves are due to the leaky Rayleigh mode. Because of the flat characteristics of the dispersion curve for Al/Si (see Fig. 18), it can be expected that the oscillations of the $V(z)$ curves in a larger region of fd will be predominantly due to the leaky-Rayleigh-wave mode. The variation of the wave form of these $V(z)$ curves is not obvious as the fd increases. However, the dotted line in Fig. 22, showing the $V(z)$ curve for a $0.6 \mu\text{m}$ thick layer, indicates that the oscillation of the $V(z)$ curve is due mainly to the leaky Sezewa mode. The contribution of the leaky Rayleigh mode causes a small fluctuation of the oscillation in the $V(z)$ curve.

Figure 23 shows another example of wave-form analysis of the $V(z)$ curve. The material combination is a silicon substrate with a thin layer of cobalt. The solid line in Fig. 23 shows the $V(z)$ curve for a specimen with a layer thickness of $0.1 \mu\text{m}$, the dashed line indicates the $V(z)$ curve for a layer thickness of $0.8 \mu\text{m}$, and the dotted line the $V(z)$ curve for a thickness of $2.0 \mu\text{m}$. In these regions of fd there are two possible leaky wave modes from the dispersion relation for the Co/Si combination: the leaky Rayleigh mode and the leaky Sezewa mode. It is clear that the oscillations of the solid line ($d = 0.1 \mu\text{m}$) are due predominantly to the leaky Rayleigh mode. This $V(z)$ curve shows regular periodic oscillations. The $V(z)$ curve of the dashed line indicates that the oscillation is caused by the leaky-Sezewa-wave mode, because the higher wave speed of the Sezewa mode causes a larger displacement of the oscillation than does a Rayleigh mode. The contribution of the leaky Rayleigh mode, which causes the small fluctuations in this $V(z)$ curve, is weak. The other $V(z)$ curve in Fig. 23 (dotted line) contains two regions, which represent the different responses for two leaky modes. The shorter and the longer intervals in oscillations of the $V(z)$ curve correspond to the leaky-Rayleigh-wave mode and the leaky-Sezewa-wave mode, respectively. The small

fluctuations in the longer-interval oscillations of the $V(z)$ curve are caused by superposition of the leaky Rayleigh mode, but their contribution to the $V(z)$ curve is weak.

From these examples and the dispersion studies of the leaky SAW we can draw several conclusions about $V(z)$ behavior for layered structures.

(1) When a layered solid is examined by a SAM, more than one leaky-SAW mode may be excited and propagated within the semiangle of the acoustic lens. Such leaky-SAW modes are excited simultaneously in the SAM and contribute to the output response $V(z)$. As a consequence, the output response of the SAM will be confused and the $V(z)$ curve will have a complex oscillatory variation; a simple periodicity in the $V(z)$ curve will no longer occur. This is the main disadvantage of using a SAM for the characterization of layered structures. The complexity of the $V(z)$ curve makes it very difficult to extract elastic properties of the specimen from the measured $V(z)$ data.

(2) Various leaky-surface-wave modes dominate the oscillations of the $V(z)$ curves for various layer thicknesses. For a small layer thickness, the most fundamental excited leaky-SAW mode is the leaky Rayleigh mode, and it makes the dominant contribution to the oscillation of the $V(z)$ curve, whereas for large thicknesses the Sezewa mode is the relevant mode.

C. Material characterization of a layered solid by surface acoustic wave dispersion

Until now, we have described the propagation characteristics of surface acoustic waves in layered solids and features of $V(z)$ for layered structures. That is, for a given model of a layered structure we have found out how to evaluate its SAW dispersion relation and to calculate its $V(z)$ curve. On the other hand, one wants to develop a new approach which can predict the structural properties of a layered solid from the measured SAW dispersion data. Such an approach and method should be very useful for developing the SAM as a diagnostic tool for material characterization. Because the SAW dispersion in a layered solid is a function of both frequency and layer thickness and elastic parameters, the material characterization of layered structures, such as the estimation of layer thickness, the determination of elastic properties, and the evaluation of cohesive properties of the bond, should be carried out by measuring their effects on SAW dispersion. From a theoretical point of view, the former is referred to as “the direct problem” (or “forward problem”), whereas the latter is referred to as “the inverse problem.”

Forward problem: model parameters → *model* → *prediction of dispersion relation*;

Inverse problem: dispersion data → *model* → *estimates of model parameters*.

The problem of determining the structural properties associated with a given set of SAW dispersion data is more complex. Analytical and exact solutions of this problem are unknown in nondestructive evaluation, except for a few very simplified examples. Based on the knowledge obtained from extensive parametric studies of theoretical models of SAW dispersion relations, it is possible to determine the unknown

parameters by matching with measured data on a trial and error method (for example, the parameter-fitting procedure by forward optimization). Unfortunately, this procedure is too inefficient to apply in practice. Therefore, using a systematic and automatic inversion scheme, for example, the iterative approach, is very desirable for attaining this goal. While the inversion problem in acoustic microscopy is a relatively new topic, studies of similar problems in geophysics date back several decades. Inversion theories and practical inversion methods have been developed by seismologists. These techniques form a valuable reference base for the inversion problem of SAW dispersion data in acoustic microscopy.

1. Layer-thickness measurement in a single-layered structure

The $V(z)$ technique lends itself to the measurement of the absolute dispersion: velocity versus product of frequency and layer thickness (see Figs. 17 and 18). Moreover, if the SAW dispersion has been measured for the layered solid examined, the layer thickness can also be found from the measured SAW dispersion data (Weglein, 1979b). That is, we first theoretically calculate the dispersion relation of the relevant SAW mode from known elastic parameters of each layer and substrate. By measuring $V(z)$ at a certain frequency and finding the corresponding SAW velocity, we can deduce the layer thickness from the theoretical dispersion relation. This technique can be applied in practice with high accuracy and without the need of standards. The drawback is that it is difficult to measure the larger layer thicknesses because multiple SAW modes are excited in a thick layered structure. The accuracy of the layer-thickness measurement is associated with the accuracy of the velocity measurement of the leaky SAW and the dispersion characteristics, i.e., the gradient of the dispersion curves, of the tested specimen. It may be expected from the dispersion curve (see Fig. 18) that a layer-thickness measurement of materials with a larger gradient in their dispersion curves will have higher resolution than a measurement of materials with a lower dispersion gradient. Furthermore, the study of the dispersion curve shows that, as the frequency increases, the gradient of the corresponding dispersion curve can also be increased. This implies that for a given layered solid the resolution of a layer-thickness measurement can be improved by the use of an appropriate higher frequency. We have estimated (Yu and Boseck, 1994) that, using the commercial Leica ELSAM system, one can obtain layer-thickness accuracies for semiconductor technology from ± 5 nm up to ± 40 nm depending on the layer/substrate combinations under test (the metal layers, cobalt, tungsten, and aluminum deposited on a Si substrate). Because of the exponential decay, a surface wave may be considered to sample the elastic properties of a layer approximately one wavelength thick. This limits the range of the layer-thickness measurement, which must be much less than the wavelength ($d < \lambda_R$) of the surface wave. The best accuracy in layer-thickness measurements in semiconductor technology is obtained by limiting the measurement range to less than 1/5–1/10 the wavelength of the surface wave.

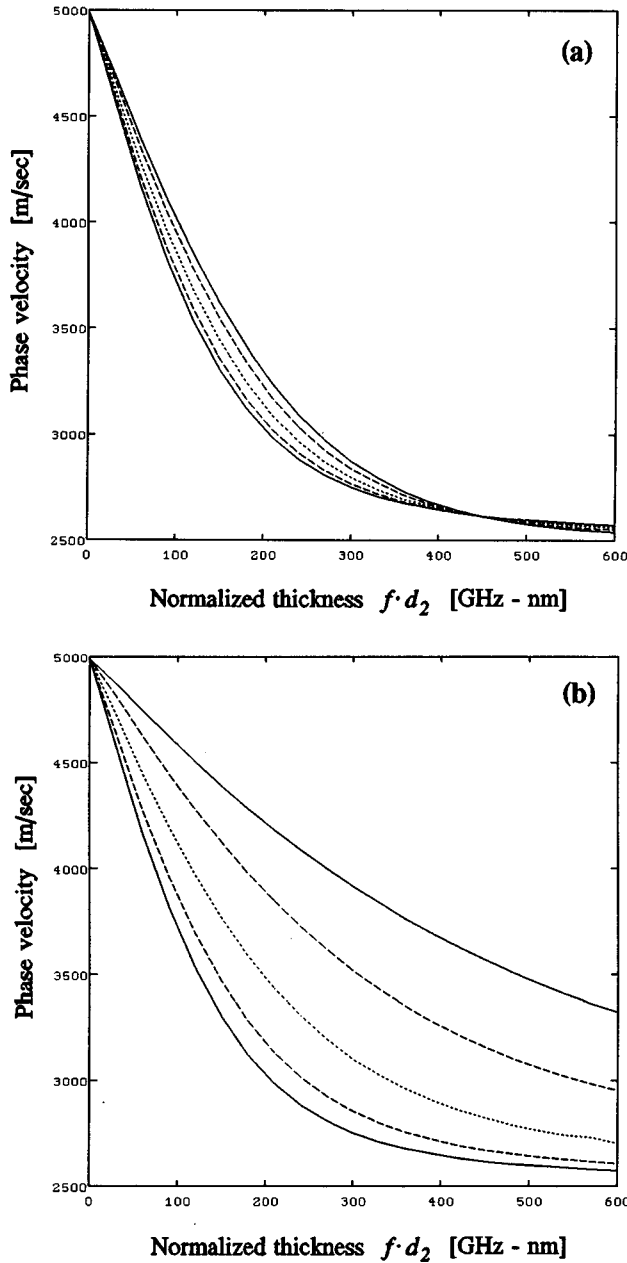


FIG. 24. SAW dispersion curves for two samples of a two-layered solid. From above to below, $d_1/d_2=0.0, 0.2, 0.5, 0.8,$ and 1.0 . (a) SAW dispersion curves for Co/W/Si; (b) SAW dispersion curves for W/Co/Si.

2. Layer-thickness measurement in a two-layered structure

This technique is useful in principle for layer-thickness measurements in a multilayered structure. However, in multilayered structures the SAW dispersion depends not only on the combination of materials but also on the different layer-thickness ratios, and the dispersion curves for different layer-thickness combinations may overlap each other in the SAW data space. Therefore it is impossible to extract more than one unknown layer thickness from a single SAW velocity. Figure 24 presents numerical examples of SAW dispersion for a two-layered solid, which were calculated by use of the traditional analytical formulation described by Farnell (see Sec. V.A) with the effective elastic constants and the effective

mass density of two layers. The effective elastic constants and the effective mass density of a superlattice have been derived in terms of the corresponding parameters of the constituent layers (Grimsditch, 1985). Their calculated formulas can be summarized as follows. Assuming that the thickness, the elastic constants, and the density of layer 1 are denoted by $d_1, C_{11}^1, C_{12}^1, C_{44}^1,$ and $\rho_1,$ respectively, those of layer 2 are denoted by $d_2, C_{11}^2, C_{12}^2, C_{44}^2,$ and $\rho_2,$ respectively. The thickness fractions of the two kinds of layers are $f_1=d_1/(d_1+d_2)$ and $f_2=d_2/(d_1+d_2),$ where (d_1+d_2) is the superlattice period. Then, the effective mass density of the superlattice is

$$\bar{\rho} = f_1\rho_1 + f_2\rho_2. \quad (29)$$

The six independent effective elastic constants for the superlattice can be given as

$$\begin{aligned} \bar{C}_{13} &= \frac{f_1 C_{12}^1 C_{11}^2 + f_2 C_{12}^2 C_{11}^1}{f_1 C_{11}^2 + f_2 C_{11}^1}, \\ \bar{C}_{33} &= [f_1/C_{11}^1 + f_2/C_{11}^2]^{-1}, \\ \bar{C}_{11} &= f_1 C_{11}^1 + f_2 C_{11}^2 + f_1 \frac{C_{12}^1}{C_{11}^1} (\bar{C}_{13} - C_{12}^1) \\ &\quad + f_2 \frac{C_{12}^2}{C_{11}^2} (\bar{C}_{13} - C_{12}^2), \\ \bar{C}_{12} &= f_1 C_{12}^1 + f_2 C_{12}^2 + f_1 \frac{C_{12}^1}{C_{11}^1} (\bar{C}_{13} - C_{12}^1) \\ &\quad + f_2 \frac{C_{12}^2}{C_{11}^2} (\bar{C}_{13} - C_{12}^2), \\ \bar{C}_{44} &= [f_1/C_{44}^1 + f_2/C_{44}^2]^{-1}, \\ \bar{C}_{66} &= f_1 C_{44}^1 + f_2 C_{44}^2. \end{aligned} \quad (30)$$

The above equations predict that the effective elastic constants do not depend on the superlattice period (d_1+d_2) but depend on the thickness ratio of the two constituent layers.

The models used in Fig. 24 are a Co layer (layer 1) on a W layer (layer 2) on a Si(100) half-space and a W layer on a Co layer on a Si(100), respectively. In Figs. 24(a) and 24(b) the SAW curves are presented for the values of the normalized thickness $fd_2,$ in which f is the frequency and d_2 is the thickness of layer 2, and the thickness d_1 of layer 1 is represented by the ratios $d_1/d_2.$ Here d_1/d_2 take as the five values 0.0, 0.2, 0.5, 0.8, 1.0.

It can be seen from Fig. 24 that the SAW dispersion curves show different negative gradients, depending on the different layer-thickness ratios for a given material combination. The dispersion curves may also overlap in the data space. The determination of layer thicknesses from those overlapped SAW data is not unique. Even if the dispersion curves for the different ratios of d_1/d_2 do not overlap each other, it is still impossible to extract the characteristics of two unknown layer thicknesses from only a single SAW velocity, since it is also not unique. One must take several $V(z)$ measurements at various frequencies to obtain more SAW dispersion data instead of measuring it at only a single frequency, and then it is necessary to use a good inversion method to predict the layer thicknesses from the SAW dispersion data obtained. We

have developed a technique for layer-thickness measurement in thin two-layered structures (Yu and Boseck, 1995). This approach is based on a modified simplex method (Nedler and Mead, 1965). When one seeks a least-squares fit of the dispersion relation between the measured data and the calculated curve, an inversion of the SAW data finally yields the unknown thicknesses of the individual layers.

3. Measurement of mechanical properties in a layered structure

It is also possible to examine the elastic constants (C_{11} , C_{12} , and C_{44}) of the layer, or residual stresses and cohesive properties of the bond, from the measured SAW dispersion data in a layered solid. This approach is nondestructive and particularly useful for the characterization of layers of as-grown films; it cannot be replaced by any other conventional analytical means. One either uses the inversion technique or obtains a computer fit from the precisely measured propagation characteristics of the relevant surface-wave mode. In order to apply this technique to the SAW dispersion data, first, it is necessary to have an analytical relationship between the measured data and the unknown parameters of the test specimen. Then, the SAW data must be precisely measured by the $V(z)$ technique at a number of frequencies. Using an iterative procedure or by computer parameter-fitting of the dispersion relation between the measured data and the calculated values, one can deduce the unknown elastic parameters of the layer materials and/or the adhesion properties at the interface from the measured SAW dispersion data (Crean *et al.*, 1987; Weglein, 1987; Kim and Achenbach, 1992; Kundu, 1992; Yu and Boseck, 1992; Lee *et al.*, 1995).

In the computer parameter-fitting method, one estimates the unknown parameters by matching the measured data on a trial and error basis. In the inversion procedure one often uses a linearization-iteration process: starting with an initial model, one solves the forward problem, then sets up linear equations for the difference between observable and calculated values for the initial model, in terms of a perturbation in model parameters; then one solves the linear equations for the perturbation, revises the initial model, and then repeats the whole process. Moreover, three aspects of the solution of an inversion problem, i.e., convergence, uniqueness, and reliability, contribute to a successful inversion procedure. Clearly, the inverse problem is intellectually challenging. Looking ahead a little further, we believe the inverse problem of SAW dispersion data in acoustic microscopy will be a good research topic for acoustic micrometrology.

VI. FURTHER DEVELOPMENTS IN SCANNING ACOUSTIC MICROSCOPY

So far in this paper, we have described the general principles and main features of acoustic microscopy and shown its application to the quantitative characterization of materials. However, the conventional SAM, also known as a point-focus-beam SAM, is equipped with a spherical lens. When one uses such a SAM to characterize anisotropic materials and thick layered structures, severe difficulties are encountered. In anisotropic materials the surface-wave velocity de-

pends on the direction of propagation. The point-focus beam excites leaky SAWs propagating in all directions, so that the acoustic properties are measured as a mean value around the beam axis. The $V(z)$ obtained for an anisotropic specimen becomes

$$V(z) = \int_0^{2\pi} \int_0^{\theta_m} P^2(\theta) u_1^2(\theta) R(\theta, \phi) \times \exp(-i2k_w z \cos\theta) \sin\theta \cos\theta d\theta d\phi, \quad (31)$$

where ϕ denotes the azimuthal angle and $R(\theta, \phi)$ is a complex reflectance function, which now is a function of the polar and azimuthal angles. As it integrates information from all azimuthal directions, the system cannot be used to detect acoustic properties that reflect crystallographic anisotropies. On the other hand, when a conventional SAM is used to image a thick layered structure, many leaky-SAW modes may be excited in a specimen and propagated within the semiangle of the acoustic lens. All such modes exist simultaneously, and the efficiency of excitation is rather low, because an appreciable part of the input power is wasted at angles where there is no subsurface excitation and only a small amount of energy can convert into SAWs. The presence of all SAW modes simultaneously also makes the images difficult to interpret. Such problems restrict extensive applications of the SAM in materials science. Further improvements in SAM performance are needed to overcome these limitations. Many authors have begun to advance research along these lines. As far as we can see, the problem of further improving SAM performance for quantitative measurements can be broken into two parts. First, and the most active area, is developing new lens types and enhancing their imaging performance. The other area is developing new kinds of scanning and of recording acoustic signatures. To show what has been achieved in these areas we briefly present several successful examples.

A. Specialized lens geometries

The lens in an SAM can be considered as the acoustic wave transformer, which transfers the bulk plane wave generated by the transducer to wave fronts in the coupling liquid. The energy is converted into surface waves directly on the surface of the specimen, and then the lens converges the reradiated surface-wave beams back to the transducer. Its construction and imaging properties (for example, its ability to transform the wave fronts, sensitivity, conversion efficiency, signal-to-noise ratio, and so on) should be further improved, in order to make it either generate a desired wave front for measurement of a property of special materials, or choose selectively a particular SAW mode with high efficiency, if it is possible to identify a leaky-SAW mode that will optimize material characterization. All of the imaging means and processes used in technical optics are available for reference and can be utilized for this purpose. Today, various acoustic lens geometries (spherical lens, line-focus-beam lens, conical lens, annular lens, and so on) have been applied to the SAM. All of these lenses have their special characteristics, their advantages and disadvantages, and can be selected for particular purposes.

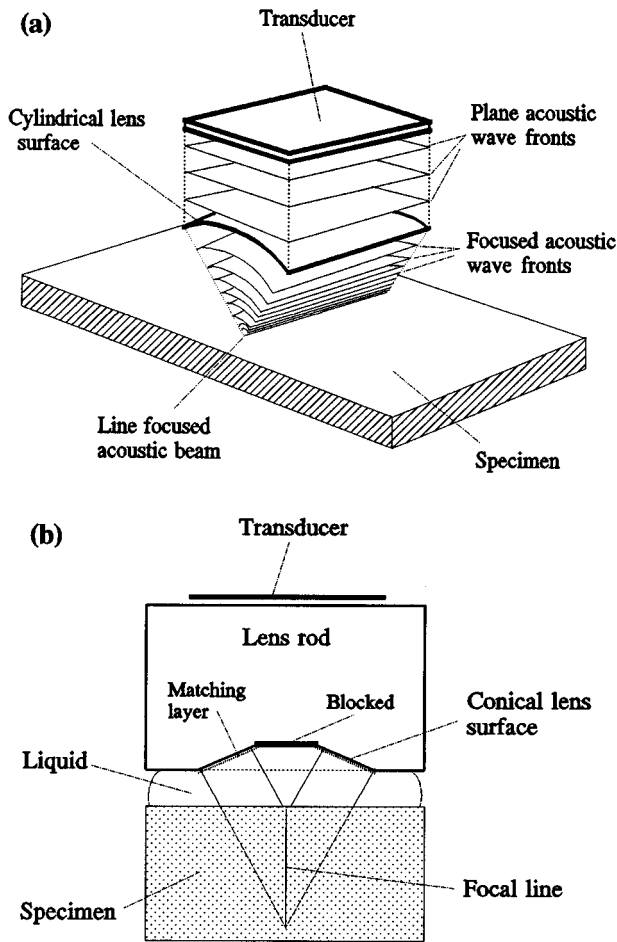


FIG. 25. (a) Wave fronts in a line-focus-beam microscope; (b) geometry of the Lamb-wave lens.

1. Line-focus-beam lens

As mentioned above, the conventional SAM is not suitable for investigation of elastic properties of anisotropic materials because the surface-wave velocity depends on the direction of propagation. In order to be able to make measurements in one direction at a time, we need to use a lens with a cylindrical surface instead of the spherical surface needed for transforming the acoustic wave fronts. This type of SAM is known as a line-focus-beam SAM (Kushibiki and Chubachi, 1985). The principle is illustrated in Fig. 25(a). The cylindrical lens produces a so-called line-focus beam, parallel to the axis of the cylindrical surface. Surface waves are excited in a direction perpendicular to the line focus. This enables elastic measurements to be made in different directions on anisotropic specimens such as wafers of electronic and optoelectronic materials. But because the line-focus-beam lens generates a focus along a line, it has poor spatial resolution in that direction. Moreover, the line-focus-beam microscope gives good azimuthal resolution, but is not suitable for imaging.

2. Lamb-wave lens

When a conventional SAM equipped with a spherical lens is used to image a layered structure, almost all possible

acoustic wave modes are simultaneously excited in the specimen, and the efficiency of excitation is rather low. To overcome this disadvantage, the logical questions naturally are: is it possible to excite only one key leaky-SAW mode for material characterization?, and is it possible to increase the excitation efficiency of that excited leaky SAW? The answer is yes. As a consequence, new lens geometries are being proposed, one of which uses a conical recessed surface geometry [see Fig. 25(b)] to replace the spherical cavity of the conventional lens. In Fig. 25(b) the acoustic waves produced by the transducer will first hit the conical refracting surface before they reach the object surface. All the refracted rays from the conical surface are incident on the object surface at the same angle. If the inclination of generated conic waves is chosen to be a critical angle for a particular mode of leaky SAW, this new lens, called a "Lamb-wave lens" (Atalar *et al.*, 1992), excites only one of the leaky-SAW modes on the layered solid and converts a large fraction of the incident energy to that leaky-SAW mode with a high efficiency. Since the leaky-surface-wave modes in the layered solid are dispersive, and their critical angles depend on frequency, the Lamb-wave lens should selectively excite the leaky mode by matching the fixed incidence angle to the corresponding critical angle by adjusting the operating frequency. The images obtained by this lens are easy to interpret and the subsurface sensitivity is high. $V(z)$ obtained with this lens is formed by the interference of a single leaky-SAW mode, and the specular reflection provides regular oscillations with periodic intervals. The drawbacks of this type of lens are twofold: identifying the order of the excited surface-wave mode is not easy in a practical specimen, and this results in difficulty in determining layer thickness from the measured SAW dispersion data. In addition, a Lamb-wave lens does not have as well-defined a focal plane as the spherical lenses, because it produces a focal line in the axial direction of the lens. Its axial resolution is equal to the thickness of the layer, since the leaky-SAW modes exist predominantly in the layer. But it is possible to obtain lateral resolutions better than a wavelength with a Lamb-wave lens. The Lamb-wave lens can complement the conventional lens in acoustic microscopy for some applications, especially subsurface imaging in layered structures.

B. Scanning alternatives and recorded functions

We have already shown that two kinds of spatial scanning can be used in acoustic microscopy, namely, x - and y -direction scanning for the purpose of imaging and z -direction scanning for $V(z)$ output. Other types of scanning may also be used in the acoustic microscope. To show this we can use an alternative approach to the acoustic material signature. Referring to the theory of $V(z)$, we may write the variation of the signal output V in the SAM as a function of different variables, such as the defocus z , the scanning frequency f , and the polar angle θ (the incident angle). We rewrite Eq. (31) as

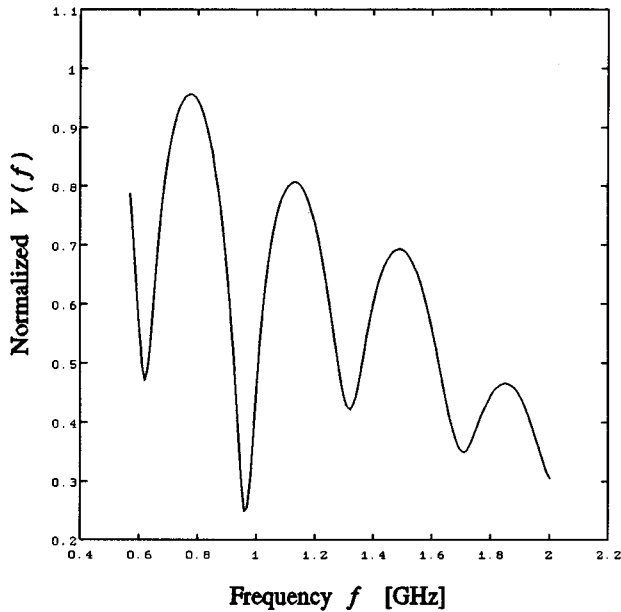


FIG. 26. $V(f)$ curve for glass sample at $z = -18.0 \mu\text{m}$.

$$V(z, f, \theta) = \int_0^{2\pi} P^2(\theta) u_1^2(\theta) R(\theta, \phi) \times \exp\left(-i4\pi z \frac{f}{v_w} \cos\theta\right) \sin\theta \cos\theta d\phi, \quad (32)$$

where $R(\theta, \phi)$ is the reflectance function of the sample (here anisotropic properties of materials are allowed). As a result, we can obtain three kinds of recorded functions for describing the signal output of a SAM: $V(z)$, $V(f)$, and $V(\theta)$, with the other variables as the parameters. The $V(z)$ function has already been described above. Here we simply describe briefly the functions $V(f)$ and $V(\theta)$.

1. $V(f)$ function

In acoustic microscopy, using frequency scanning instead of z -direction scanning, one may obtain a $V(f)$ function in the frequency domain (Nagy and Adler, 1990). We consider the case of the conventional SAM and start from Eq. (32). Because the spherical lens excites all polar angles θ at the object interface, we need only to consider $V(z, f)$ in Eq. (32). From this integral we see that the defocusing z is measured in terms of the acoustic wavelength v_w/f . Therefore it always appears as a product with frequency f . $V(f)$ is a particular cross section of $V(z, f)$ in Eq. (32) at a certain defocusing depth, while $V(z)$ is simply the cross section of $V(z, f)$ at a certain frequency. The interchangeability of z and f in the material signature of the specimen gives us the option of analyzing the frequency spectrum of the received signal rather than its z dependence. In practical operation, as the frequency is scanned while z is kept constant, a characteristic $V(f)$ curve is traced. The $V(f)$ characterization is similar to the $V(z)$ effect. For example, for a nonlayered smooth solid the $V(f)$ curve exhibits more-or-less periodicity. Figure 26 shows a calculated $V(f)$ curve for a glass sample at $z = -18.0 \mu\text{m}$.

The $V(f)$ approach has some advantages over the $V(z)$ approach. For example, scanning in the frequency domain can be done electronically, which is much simpler, smoother, and faster than the z -direction mechanical translation of the whole transducer assembly, as is required for the $V(z)$ method. Moreover, the interpretation of $V(f)$ is easier than that of $V(z)$. Of course, in $V(f)$ operation it is necessary to use broadband ultrasonic transducers. In addition, for a layered structure the $V(f)$ curves present additional difficulties for quantitative evaluation, since strong surface-wave dispersion occurs in this case. Thus one must use a particular lens construction, for example a Lamb-wave lens, to obtain a useful $V(f)$ curve for the characterization of layered structure. In this case the $V(f)$ curve results in peaks at positions corresponding to different leaky-SAW modes excited in the sample.

2. $V(\theta)$ function

When the polar angle is scanned, the SAM signal received is plotted as a function of incidence angle θ , and the resulting curve can be called a $V(\theta)$ curve (Atalar *et al.*, 1988). This kind of scanning can be performed using Lamb-wave lenses with various conical angles. The $V(\theta)$ effect can be used to deduce the relative sensitivities of the excited leaky-SAW modes and to find the most sensitive excitation angle (i.e., the most sensitive surface-wave mode). This allows us to detect a particular defect in a layered structure.

Other scanning versions are also possible. For example, a line-focus-beam SAM can be considered as a combination of z -direction spatial scanning and discrete azimuthal angle scanning (ϕ direction), which is sensitive to the directional properties of anisotropic materials. Therefore, developing new scanning versions and recorded forms should be of great significance in enhancing the performance of the SAM.

Finally, it must be pointed out that efficient processing techniques for the output data in a SAM are also important for obtaining accurate quantitative evaluations. Research in this direction is an area of great activity (Briggs *et al.*, 1988; Kanai *et al.*, 1992).

VII. SUMMARY

Nondestructive evaluation of near-surface properties of materials is usually carried out using acoustic techniques. Bulk acoustic waves fail in this case, due to their large reflection at the boundary and their very weak acoustic contrast, so that even very different materials are difficult to distinguish. In contrast, surface acoustic waves have been successfully used for near-surface evaluation of materials, because they extend beneath the surface and are very sensitive to surface inhomogeneities. Several acoustic systems based on surface acoustic waves have been proposed for imaging. Scanning acoustic microscopy, among others, has been successfully developed, and it would appear to be one of the most promising means for the evaluation of physical properties of materials. In many applications acoustic microscopy will be used in conjunction with conventional microscopic techniques (such as optical and electron). There are, however, some applications for which acoustic microscopy is uniquely suited. Such applications are the imaging of

the interior of optically opaque objects and the quantitative evaluation of elastic properties of materials on a microscopic scale.

In a brief review such as this paper it is impossible to describe all details of the acoustic microscope and to cover all the latest developments in acoustic microscopy. We have covered areas that we think are essential for understanding acoustic microscopy and its applications to material characterization. We have first explained that in the scanning acoustic microscope the acoustic image of an object under test is obtained by mechanical scanning. Because of the use of mechanical scanning, the acoustic lens must perform well only on axis. It is this feature that has made it possible to record high-quality acoustic images with submicrometer resolution. Since the resolving power of an acoustic lens is primarily constrained by the operating frequency, increasing the frequency improves the resolution. On the other hand, the ability to image below the surface of materials, another attractive property of acoustic microscopy, is also affected by frequency. Penetration ability has been estimated to be about the same magnitude as the wavelength of the surface acoustic wave excited in a specimen. Increasing the frequency reduces the penetrating ability due to the increase in the acoustic attenuation of samples with frequency. Therefore resolution and penetration must be traded off.

We have further shown that the image contrast observed in acoustic microscopy is related to elastic properties near the surface as well as below the surface of the sample. Thus, we have a probe that is not comparable with any other kind of microscopy. The interpretation of the contrast is a major task and of essential interest for an acoustic microscopist. When the acoustic lens is focused at the surface of the specimen, only specular reflection is generated, and the acoustic contrast is very weak. When, however, the lens is focused below the surface the contrast becomes much stronger. Especially in defocusing scanning, a series of oscillations in the transducer output is observed. This effect is known as the acoustic material signature or, simply, the $V(z)$ curve, and it is a function of the defocus z . $V(z)$ is an interference result between the nonspecularly reflected surface acoustic waves excited in the specimen and specularly reflected waves. Its theory can be classified into two general categories: those involving Fourier angular spectrum analysis and those based on ray optical models. The shapes of $V(z)$ curves are unique and characteristic of materials; from them one can extract quantitative information on acoustic properties in materials with microscopic precision. In the rapid development of acoustic microscopy, the $V(z)$ effect has played a very important role in both acoustic imaging and quantitative measurements for the nondestructive evaluation of materials.

Knowledge of the propagation properties of surface acoustic waves on the surface of materials is essential for understanding contrast mechanisms and for quantitative applications in acoustic microscopy. Thus we have also described the propagation characteristics of surface acoustic waves in nonlayered smooth and layered solids, and then examined their effect on the behavior of $V(z)$. A surface acoustic wave excited in a nonlayered smooth solid is only a single, non-dispersive mode, namely, a Rayleigh wave. When a nonlayered specimen is imaged by the acoustic microscope, the

obtained image is simple, and a series of regular periodic oscillations occurs in its output response $V(z)$. This kind of image and the $V(z)$ curve can be easily interpreted. On the other hand, in layered structures more than one surface wave mode, such as Rayleigh-like modes, Sezewa modes, and Love modes, can be excited, and they are dispersive. When this kind of specimen is examined by the acoustic microscope, many surface waves make contributions to the output response. As a consequence, the $V(z)$ curve has a complex variation and will no longer exhibit a simple periodicity. Extracting the elastic properties of the specimen from the measured $V(z)$ data may become rather complicated. In order to determine the elastic properties of a layered structure from the relevant surface-wave mode, we must carry out waveform analysis of the oscillation characteristics in the obtained $V(z)$ curve.

Applications of acoustic microscopy are growing so fast that it is impossible to keep up with them all. The applications presented here have given only a slight indication of the scope of nondestructive evaluation in solid materials. The main results can be summarized as follows: the full reflectance function R of a specimen is deduced by inverting the measured $V(z)$ data; phase velocity and attenuation of surface waves on the liquid-specimen boundary are determined through the $V(z)$ measurement; elastic constants of bulk materials are estimated by analyzing the velocities of surface waves excited in the specimens; for layered structures, layer thicknesses and mechanical properties can also be evaluated by measuring the dispersion properties of surface waves, through the use of an inversion procedure and computer parameter-fitting techniques. The applications of acoustic microscopy to biology and the imaging of subsurface features in materials are no doubt very important application areas, which have not been presented here for simplicity.

Finally, we have indicated that because the conventional acoustic microscope is equipped with a spherical lens, when one uses such an acoustic microscope to characterize thick layered structures and anisotropic materials, difficulties arise. In the case of thick layered structures, the presence of many surface-wave modes makes interpretation of the images rather difficult. In the case of anisotropic materials, a SAM cannot detect the acoustic properties that reflect directional anisotropies. This paper has mentioned some successful improvements in the acoustic microscope, such as the design of new lens types and development of new scanning methods, to overcome these limitations.

It is interesting to note that, although surface waves extend beneath the surface of materials and are sensitive to variations under the surface of the material, their penetration ability is limited by the wavelength of the surface wave. A lower frequency of operation results in a higher penetration but lower resolution. On the other hand, a material involving layers supports many other waves than the Rayleigh-like waves, such as Love waves and Stoneley waves. It is possible to excite these waves selectively from the liquid side if the incidence angle of the bulk wave in the liquid is properly adjusted. The resulting wave will be focused just like the Rayleigh-like waves. Using this mechanism, it should be possible to get much deeper penetration than is possible using Rayleigh-like waves.

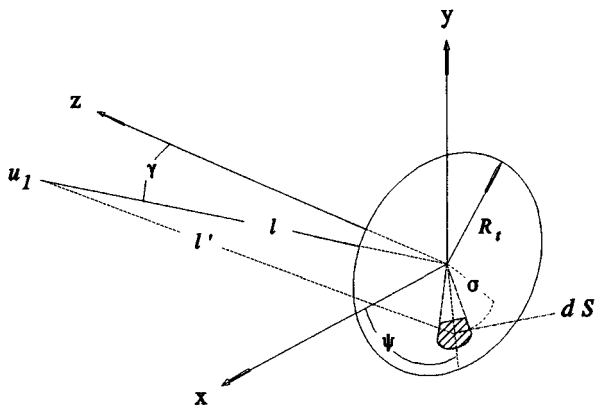


FIG. 27. Coordinate system used to calculate the acoustic field of a flat circular vibrating piston.

ACKNOWLEDGMENTS

One of us, Z. Yu, would like to thank Professor J. Graul, University of Hannover, for his continuous support and encouragement. This research was supported by DFG under grants Bo 499/8-1 and Gr 900/3-1.

APPENDIX A: ACOUSTIC FIELD $u_1(\theta)$ AT THE BACK SIDE OF THE LENS AND GENERALIZED PUPIL FUNCTION $P(\theta)$

1. Acoustic field $u_1(\theta)$ at the back side of the lens

The acoustic field $u_1(\theta)$ at the back side of the acoustic lens in a SAM (see Fig. 10) can be calculated by the diffraction theory of the piston transducer. In this appendix we shall give its expression.

The complete description of the acoustic field produced by an acoustic transducer is generally divided into two separate parts. One part of the description is limited to the region in the neighborhood of the transducer, the near-field region. The other part of the description is limited to the far-field region, the region beyond the near field. The usual definition of the near-field region is that portion of the acoustic field characterized by interference phenomena. This is also referred to as the Fresnel diffraction region. In contrast to the near-field definition, the far-field region is characterized by an interference-free acoustic field. This is the Fraunhofer diffraction region. Usually, the expression for the acoustic field within the near field is relatively complex. For this reason, theoretical studies have avoided the near-field region, and one has often used the Fraunhofer far-field approximation. In practice, however, one wants adequately to predict the performance of the transducer for operation within the near field. Here, we shall follow Zemanek's work (1971) and get the acoustic field of the back side of the lens by using the near-field description.

Although both longitudinal and shear waves are generated in the sapphire rod (see Fig. 2), we need only consider the effect of longitudinal waves, as the receiving transducer will be primarily sensitive to these waves. Figure 27 shows the coordinates of the transducer being considered. The transducer configuration is a flat circular piston. The transducer

has radius R_t and vibrates with simple harmonic motion normal to its face. The observation point will be a function of l , the radial distance from the observation point to the center of the transducer, and γ , the angle between the transducer axis and the radial vector. The field at the observation point will be the total contribution from incremental areas of the transducer. The total acoustic field can be written as (Ocheltree and Frizzell, 1989)

$$u_1 = \frac{i\rho\nu k}{2\pi} U_0 \int_S \frac{e^{-ikl' - \zeta l'}}{l'} dS$$

$$= \frac{i\rho\nu k}{2\pi} U_0 \int_0^{R_t} \left(\int_0^{2\pi} \frac{e^{-ikl' - \zeta l'}}{l'} d\psi \right) \sigma d\sigma, \quad (\text{A1})$$

where ρ and ν are density of the medium and velocity of sound in the buffer rod, respectively; U_0 is the amplitude generated by the transducer and, in the discussion that follows, can be assumed to be 1 for simplicity; S is the total area of the transducer; l' is the distance from the observation point to the incremental area; and ζ is the attenuation coefficient of sound in the buffer rod. In Eq. (A1) the time dependence $e^{-i\omega t}$ has been suppressed. The distance l' is equal to

$$l' = (l^2 + \sigma^2 - 2l\sigma \sin \gamma \cos \psi)^{1/2}. \quad (\text{A2})$$

If l' is substituted into Eq. (A1), the resulting expression is so complicated that a closed-form analytical solution cannot be obtained. However, in order to investigate the near-field description, we can evaluate Eq. (A1) numerically, without approximations, on a computer. The field u_1 is calculated for points located on a grid in the $x-z$ plane at the back side of the lens. The transducer axis corresponds to the z coordinate, and the orthogonal axis is the x coordinate. Equation (A1) is evaluated, ignoring the constant factor in front of the integral, as a double summation of contributions from elemental areas of the transducer:

$$u_1(Z, X) = \left[\sum_{p=1}^m \sum_{q=1}^n \frac{1}{L_{pq}} \exp \left\{ -i2\pi \left(\frac{R_t}{\lambda} \right)^2 L_{pq} \right\} \Delta S_q \right], \quad (\text{A3})$$

where the attenuation ζ was negligible for simplicity. Each length variable is normalized by a factor R_t^2/λ and is dimensionless, so from Eq. (A1) to Eq. (A3) one has $k = 2\pi/\lambda \Rightarrow 2\pi/\{\lambda/(R_t^2/\lambda)\} = 2\pi(R_t/\lambda)^2$. Moreover, the radial direction of the transducer is divided into n increments, and the azimuthal direction is divided into m parts,

$$n = 4R_t/\lambda,$$

$$m = n\pi. \quad (\text{A4})$$

By defining n and m in the above manner, one divides the transducer into $32\pi(R_t/\lambda)^2$ increments. This is the minimum number of increments that can be used in order to obtain results within 0.5% of results obtained using a far greater number of increments.

Thus in Eq. (A3) we have

$$\begin{aligned} \Delta S_q(\text{the elemental area}) &= \sigma_q \Delta \sigma \Delta \psi, \\ \Delta \sigma &= [R_t / (R_t^2 / \lambda)] / n = \frac{1}{n R_t / \lambda}, \\ \Delta \psi &= \pi / m, \\ \sigma_q &= \Delta \sigma \left(q - \frac{1}{2} \right), \end{aligned} \tag{A5}$$

and

$$\begin{aligned} L_{pq} &= (L^2 + \sigma_q^2 - 2L\sigma_q \sin \gamma \cos \psi_p)^{1/2}, \\ L &= (Z^2 + X^2)^{1/2}, \\ Z &= \frac{z}{R_t^2 / \lambda}, \\ X &= \frac{x}{R_t^2 / \lambda}, \\ \gamma &= \tan^{-1}(X/Z), \\ \psi_p &= \Delta \psi \left(p - \frac{1}{2} \right). \end{aligned} \tag{A6}$$

By relating the coordinates of the observation point, which is located on a grid in the $x-z$ plane at the back side of the lens, to the incidence angle θ of the acoustic wave, one may describe u_1 as a function of θ , $u_1(\theta)$.

2. Generalized pupil function $P(\theta)$

The generalized pupil function $P(\theta)$ can be expressed by (Wickramasinghe, 1979)

$$P(\theta) = \text{circ}\left(\frac{r}{r_0}\right) \exp[ikw(\theta)] \frac{\exp[-\zeta_w L(\theta)]}{L(\theta)} T(\theta), \tag{A7}$$

where $\text{circ}(r/r_0)$ is a geometrical aperture function and r_0 is the radius of the lens aperture. The second factor represents a phase correction term due to the spherical aberration of the lens, $w(\theta)$ being the wave-front error in wavelengths corresponding to the angle θ . The effects of absorption and diffraction in the coupling liquid are included in the factor $\exp[-\zeta_w L(\theta)]/L(\theta)$, where $L(\theta)$ is the distance from a striking point of the acoustic ray at the specimen surface to a point on the lens surface corresponding to θ , and ζ_w is the attenuation coefficient in the liquid. Finally, the factor $T(\theta)$ represents the complex amplitude transmittance function of the antireflection layer on the lens surface, whose thickness may vary because of the deposition procedure.

Following Lemons (1975, 1979), we find that $w(\theta)$ is very small, so $\exp[ikw(\theta)]$ can be approximated to 1. The effect of the factor $\exp[-\zeta_w L(\theta)]/L(\theta)$ can also be neglected because of the very small absorption and diffraction differences for different acoustic rays in water. Therefore the pupil function P may primarily be calculated by the factor $T(\theta)$ and can be approximately expressed by

$$P(\theta) \cong \text{circ}\left(\frac{r}{r_0}\right) T(\theta). \tag{A8}$$

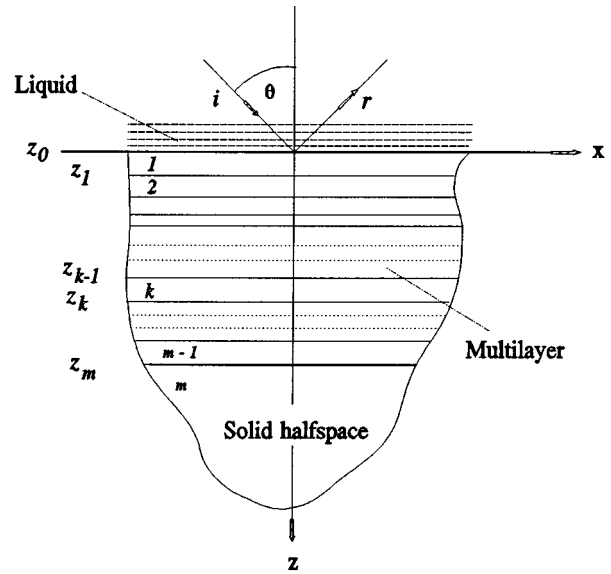


FIG. 28. Geometry of a multilayered solid overcovered by a liquid.

APPENDIX B: FORMULATION OF REFLECTANCE FUNCTION $R(\theta)$ IN A MULTILAYERED SOLID

The reflectance function R can be solved for by using different methods. For a layered solid, a widely used approach to calculating these quantities is the Thompson-Haskell method (Thomson, 1950; Haskell, 1953). This approach is based on the use of recurrence formulas, which connect the amplitude of waves in adjacent layers. Here we shall follow this approach and give a general description after some reformulations (Yu, 1991).

Consider a horizontally layered, elastic half-space as shown in Fig. 28. Each layer is assumed to be isotropic, homogeneous, and perfectly elastic. This structure is submerged in a liquid from which a plane longitudinal acoustic wave is incident. Let the coordinate system be chosen so that the x coordinate is parallel to, and the z coordinate is perpendicular to, the layer whose origin is located at the interface between the top layer and the liquid. The k_{th} layer is bounded above by the plane $z = z_{k-1}$ and below by the plane $z = z_k$, its thickness is d_k , its density is ρ_k , and it has P -wave (longitudinal, primary) and S -wave (shear, secondary) velocities of α_k and β_k , respectively. The velocity of the longitudinal wave in the liquid is v_w , and the other corresponding properties in the liquid are denoted by the subscript w . A plane acoustic wave of amplitude 1 is incident on the liquid-solid interface at an angle θ_w . We are interested in computing the total reflected field in the liquid.

In each of the layers a pair of P waves (propagating symmetrically above and below the horizontal plane) and a pair of similar S waves will appear. In the lower half-space of the solid there will be only downward traveling P and S waves.

We now consider layer k as an example. The P - and S -wave potentials in the k_{th} layer satisfy the usual wave equations and have the representations (Brekhovskikh, 1980)

$$\begin{aligned} \phi_k &= [a_k e^{-i\eta_{\alpha k}(z-z_{k-1})} + b_k e^{i\eta_{\alpha k}(z-z_{k-1})}] e^{i(\xi x - \omega t)}, \\ \psi_k &= [c_k e^{-i\eta_{\beta k}(z-z_{k-1})} + d_k e^{i\eta_{\beta k}(z-z_{k-1})}] e^{i(\xi x - \omega t)}, \end{aligned} \tag{B1}$$

in which ω denotes the circular frequency and ξ is the x component of the wave number. It follows that

$$\xi = k_w \sin \theta_w = k_{\alpha k} \sin \theta_k = k_{\beta k} \sin \gamma_k, \quad (\text{B2})$$

where

$$k_w = \omega / \nu_w, \quad k_{\alpha k} = \omega / \alpha_k, \quad k_{\beta k} = \omega / \beta_k. \quad (\text{B3})$$

k_w is the complex wave number for the P wave in the liquid, and $k_{\alpha k}$ and $k_{\beta k}$ are the complex wave numbers for the P - and S -wave vectors making acute angles θ_k and γ_k , respectively, with the z axis. The z components of the P - and S -wave vectors, $\eta_{\alpha k}$ and $\eta_{\beta k}$ in Eq. (B1), are defined by

$$\eta_{\alpha k}^2 = k_{\alpha k}^2 - \xi^2, \quad \eta_{\beta k}^2 = k_{\beta k}^2 - \xi^2. \quad (\text{B4})$$

In Eq. (B1) the coefficients a_k, b_k, c_k, d_k are unknown constants to be determined from the interface and boundary conditions. All the waves contain one common factor $e^{i(\xi x - \omega t)}$ which we shall omit for brevity.

(1) Let $u_k, v_k, \sigma_k, \tau_k$ denote the tangential and normal components of displacement and stress vectors for the k_{th} layer. In a linear, homogeneous, isotropic medium, from Brekhovskikh (1980), u_k, v_k, σ_k , and τ_k are related to the wave potentials ϕ and ψ as

$$\begin{Bmatrix} u_k \\ v_k \end{Bmatrix} = \begin{bmatrix} \partial/\partial x - \partial/\partial z \\ \partial/\partial z + \partial/\partial x \end{bmatrix} \begin{Bmatrix} \phi_k \\ \psi_k \end{Bmatrix} \quad (\text{B5})$$

and

$$\begin{Bmatrix} \sigma_k \\ \tau_k \end{Bmatrix} = \begin{bmatrix} \lambda \nabla^2 + 2\mu \partial^2/\partial z^2 & 2\mu \partial^2/\partial x \partial z \\ 2\mu \partial^2/\partial x \partial z & \mu(\partial^2/\partial x^2 - \partial^2/\partial z^2) \end{bmatrix} \begin{Bmatrix} \phi_k \\ \psi_k \end{Bmatrix}, \quad (\text{B6})$$

where λ and μ are the Lamé constants, and the Laplacian ∇^2 denotes $(\partial^2/\partial x^2 + \partial^2/\partial z^2)$. The calculation results can be written in matrix notation as

$$\begin{Bmatrix} u_k \\ v_k \\ \sigma_k \\ \tau_k \end{Bmatrix} = [Q(k)][E(z - \zeta)] \begin{Bmatrix} c_k \\ a_k \\ b_k \\ d_k \end{Bmatrix}, \quad (\text{B7})$$

where ζ could be an arbitrary constant, the 4×4 matrix $[Q]$ is given as

$$[Q(k)] = \begin{bmatrix} i\eta_{\beta k} & i\xi & i\xi & -i\eta_{\beta k} \\ i\xi & -i\eta_{\alpha k} & i\eta_{\alpha k} & i\xi \\ 2\mu_k \eta_{\beta k} \xi & \mu_k(2\xi^2 - k_{\beta k}^2) & \mu_k(2\xi^2 - k_{\beta k}^2) & -2\mu_k \eta_{\beta k} \xi \\ -\mu_k(2\xi^2 - k_{\beta k}^2) & 2\mu_k \eta_{\alpha k} \xi & -2\mu_k \eta_{\alpha k} \xi & -\mu_k(2\xi^2 - k_{\beta k}^2) \end{bmatrix}, \quad (\text{B8})$$

and $[E(z)]$ is the diagonal matrix

$$[E(z)] = \text{diag}(e_{\beta}^-, e_{\alpha}^-, e_{\alpha}^+, e_{\beta}^+) \quad (\text{B9})$$

with

$$e_{\alpha, \beta}^{\pm} = e^{\pm iz \eta_{\alpha, \beta}}. \quad (\text{B10})$$

Let

$$\{S_k\} = \begin{Bmatrix} u_k \\ v_k \\ \sigma_k \\ \tau_k \end{Bmatrix}, \quad \{C(k)\} = \begin{Bmatrix} c_k \\ a_k \\ b_k \\ d_k \end{Bmatrix}. \quad (\text{B11})$$

$\{S\}$ is called the displacement stress vector, and $\{C\}$ is an unknown constant vector. Then, within the k_{th} layer, Eq. (B7) can be expressed in the form

$$\{S_k(z)\} = [Q(k)][E(z - z_{k-1})]\{C(k)\}, \quad z_{k-1} < z < z_k. \quad (\text{B12})$$

(2) Now, we proceed to find an transfer matrix that relates $\{S(z)\}$ evaluated at the top of a layer to that function evaluated at the bottom of the layer. We utilize the conditions of continuity of displacement and stress components at the layer interfaces $z = z_{k-1}$, which is expressed by

$$\{S_k(z_{k-1})\} = \{S_{k-1}(z_{k-1})\}. \quad (\text{B13})$$

From Eq. (B12)

$$\{S_k(z_{k-1})\} = [Q(k)][E(z_{k-1} - z_{k-1})]\{C(k)\}, \quad (\text{B14})$$

so

$$\{S_{k-1}(z_{k-1})\} = [Q(k)]\{C(k)\}. \quad (\text{B15})$$

Since the matrix $[Q(k)]$ is not singular, the above equation (B15) can be solved for $\{C(k)\}$,

$$\{C(k)\} = [Q(k)]^{-1}\{S_{k-1}(z_{k-1})\}, \quad (\text{B16})$$

which can then be substituted into Eq. (B12) to yield

$$\{S_k(z_k)\} = [Q(k)][E(z_k - z_{k-1})][Q(k)]^{-1}\{S_{k-1}(z_{k-1})\}. \quad (\text{B17})$$

Let

$$[P(k)] = [Q(k)][E(d_k)][Q(k)]^{-1}, \quad (\text{B18})$$

where $d_k = z_k - z_{k-1}$ is the thickness of the k_{th} layer, so

$$\{S_k(z_k)\} = [P(k)]\{S_{k-1}(z_{k-1})\}. \quad (\text{B19})$$

This is the transfer relation of $\{S(z)\}$ evaluated at the top of a layer and the bottom of the layer, respectively. The $[P(k)]$ matrix is called the Thomson-Haskell layer matrix.

(3) Next, by successively applying the interface continuity conditions, one can relate the displacement stress vector at the k_{th} layer to that at the top surface. Similarly, the displace-

ment stress vector is related to the bottom half-space. That is, by successively applying Eqs. (B19) and (B13), we get

$$\{S_{m-1}(z_{m-1})\} = [P(m-1)][P(m-2)] \dots [P(k+1)] \\ \times [P(k)][P(k-1)] \dots [P(1)]\{S(0)\}. \quad (\text{B20})$$

From Eqs. (B16) and (B20) we can obtain

$$\{C(m)\} = [Q(m)]^{-1}\{S_{m-1}(z_{m-1})\} \\ = [Q(m)]^{-1}[P(m-1)] \\ \times [P(m-2)] \dots [P(1)]\{S(0)\}, \quad (\text{B21})$$

or

$$\{C(m)\} = [J(m,1)]\{S(0)\}, \quad (\text{B22})$$

where $[J]$ is the chain product of the layer matrices

$$[J(m,1)] = [Q(m)]^{-1}[P(m-1)][P(m-2)] \dots [P(k \\ + 1)][P(k)][P(k-1)] \dots [P(1)]. \quad (\text{B23})$$

This is a most important transfer formula.

(4) Finally, we proceed to the problem of seeking the reflectance function R . Since no S wave occurs in the liquid, ψ_w is identically zero. The wave potentials in the liquid are given by

$$\phi_w = e^{i\eta_w z} + R e^{-i\eta_w z}, \\ \psi_w = 0, \quad (\text{B24})$$

where

$$\eta_w^2 = k_w^2 - \xi^2, \quad (\text{B25})$$

and R is the reflectance function because the amplitude of the incident wave is assumed to equal 1.

From the boundary condition at the liquid-solid interface we have $\tau_0 = 0$ (i.e., the normal component of the stress vector in the liquid is null). Then by making use of Eqs. (B24), (B7), (B8), (B9), and $\mu = 0$ in the liquid, we can derive $\{S(0)\}$ as

$$\{S(0)\} = [u_0, \nu_0, \sigma_0, 0]^T \\ = [u_0, i\eta_w(1-R), -\rho_w \nu_w^2 k_w^2 (1+R), 0]^T. \quad (\text{B26})$$

On the other hand, there will be only downward-traveling waves in the lower half-space of the solid. The radiation condition in the solid half-space $z > z_{m-1}$ implies that

$$a_m = c_m = 0. \quad (\text{B27})$$

Thus we have

$$\{C(m)\} = [0, 0, b_m, d_m]^T. \quad (\text{B28})$$

We substitute these relations into Eq. (B22) to give

$$\begin{Bmatrix} 0 \\ 0 \\ b_m \\ d_m \end{Bmatrix} = [J] \begin{Bmatrix} u_0 \\ i\eta_w(1-R) \\ -\rho_w \nu_w^2 k_w^2 (1+R) \\ 0 \end{Bmatrix}, \quad (\text{B29})$$

where $[J]$ is given in Eq. (B23).

The above matrix equation (B29) gives four independent linear equations for the four unknowns b_m , d_m , u_0 , and R . The first two equations are

$$J_{11}u_0 + J_{12}i\eta_w(1-R) - J_{13}\rho_w \nu_w^2 k_w^2 (1+R) = 0, \\ J_{21}u_0 + J_{22}i\eta_w(1-R) - J_{23}\rho_w \nu_w^2 k_w^2 (1+R) = 0, \quad (\text{B30})$$

where J_{kl} is the (k, l) element of the matrix $[J]$. Eliminating u_0 from the above equations, one can obtain the reflectance function R as

$$R = \frac{\eta_w(J_{11}J_{22} - J_{12}J_{21}) + i\rho_w \nu_w^2 k_w^2 (J_{11}J_{23} - J_{21}J_{13})}{\eta_w(J_{11}J_{22} - J_{12}J_{21}) - i\rho_w \nu_w^2 k_w^2 (J_{11}J_{23} - J_{21}J_{13})}, \quad (\text{B31})$$

or in the closed form

$$R = (\eta_w J_{22}^{11} + i\rho_w \omega^2 J_{23}^{11}) / (\eta_w J_{22}^{11} - i\rho_w \omega^2 J_{23}^{11}), \quad (\text{B32})$$

where $\omega = \nu_w k_w$ is the circular frequency and

$$J_{kl}^{ij} = J_{ij}J_{kl} - J_{il}J_{kj}. \quad (\text{B33})$$

The indices i, j, k, l in Eq. (B33) take on the values 1, 2, 3, 4.

REFERENCES

- Atalar, A., 1978, *J. Appl. Phys.* **49**, 5130.
 Atalar, A., 1985, *IEEE Trans.* **SU-32**, 164.
 Atalar, A., 1989, *IEEE Trans. Ultrason. Ferroelect. Freq. Contr.* **36**, 264.
 Atalar, A., H. Köymen, and F. L. Değertekin, 1992, *IEEE Trans. Ultrason. Ferroelect. Freq. Contr.* **39**, 661.
 Atalar, A., H. Köymen, and O. Yemişçiler, 1988, in *IEEE 1988 Ultrasonics Symposium, Proceedings*, edited by B. R. McAvoy (IEEE, New York), Vol. 2, p. 771.
 Auld, B. A., 1973, *Acoustic Fields and Waves in Solids* (Wiley, New York).
 Bertoni, H. L., 1984, *IEEE Trans.* **SU-31**, 105.
 Bertoni, H. L., and T. Tamir, 1973, *Appl. Phys.* **44**, 48.
 Block, H., G. Heygster, and S. Boseck, 1989, *Optik* **82**, 147.
 Bogy, D. B., and S. M. Gracewski, 1983, *J. Acoust. Soc. Am.* **74**, 591.
 Born, M., and E. Wolf, 1972, *Principles of Optics* (Pergamon, Oxford, New York).
 Brekhovskikh, L. M., 1980, *Waves in Layered Media* (2nd edition) (Academic, New York).
 Briggs, G. A. D., 1985, *An Introduction to Scanning Acoustic Microscopy*, Royal Microscopical Society Handbook (Oxford University, Oxford).
 Briggs, G. A. D., 1992, *Acoustic Microscopy* (Clarendon, Oxford).
 Briggs, G. A. D., J. M. Rowe, A. M. Sinton, and D. S. Spencer, 1988, in *IEEE 1988 Ultrasonics Symposium, Proceedings*, edited by B. R. McAvoy (IEEE, New York), Vol. 2, p. 743.
 Chimenti, D. E., A. H. Nayfeh, and D. L. Butler, 1982, *J. Appl. Phys.* **53**, 170.
 Crean, G. M., A. Golanski, and J. C. Oberlin, 1987, *Appl. Phys. Lett.* **50**, 74.
 Farnell, G. W., and E. L. Adler, 1972, in *Physical Acoustics* Vol. 9, edited by W. P. Mason and R. N. Thurston (Academic, New York), p. 35.
 Fright, W. R., R. H. T. Bates, J. M. Rower, D. S. Spencer, M. G. Somekh, and G. A. D. Briggs, 1989, *J. Microsc.* **153**, 103.
 Grimsditch, M., 1985, *Phys. Rev. B* **31**, 6818.

- Goos, F., and H. Hänchen, 1947, *Ann. Phys. (Leipzig)* **1**, 333.
- Hadimioglu, B., and J. S. Foster, 1984, *J. Appl. Phys.* **56**, 1976.
- Hammer, R., and R. L. Hollis, 1982, *Appl. Phys. Lett.* **40**, 678.
- Haskell, N. A., 1953, *Bull. Seism. Soc. Am.* **43**, 17.
- Hoppe, M., and J. Bereiter-Hahn, 1985, *IEEE Trans. SU-32*, 289.
- Kanai, H., N. Chubachi, and T. Sannomiya, 1992, *IEEE Trans. Ultrason. Ferroelect. Freq. Contr.* **39**, 643.
- Kim, J. O., and J. D. Achenbach, 1992, *J. Appl. Phys.* **72**, 1805.
- Kino, G. S., 1987, *Acoustic Waves: Devices, Imaging and Analog Signal Processing* (Prentice-Hall, Englewood Cliffs, New Jersey).
- Kundu, T., 1992, *J. Acoust. Soc. Am.* **91**, 591.
- Kundu, T., A. K. Mal, and R. D. Weglein, 1985, *J. Acoust. Soc. Am.* **77**, 353.
- Kushibiki, J., and N. Chubachi, 1985, *IEEE Trans. SU-32*, 189.
- Kushibiki, J., T. Ueda, and N. Chubachi, 1987, in *IEEE 1987 Ultrasonics Symposium Proceedings*, edited by B. R. McAvoy (IEEE, New York), Vol. 2, p. 817.
- Lee, Y. C., J. O. Kim, and J. D. Achenbach, 1995, *IEEE Trans. Ultrason. Ferroelect. Freq. Contr.* **42**, 253.
- Lemons, R. A., 1975, Ph.D. thesis (Stanford University).
- Lemons, R. A., and C. F. Quate, 1974, *Appl. Phys. Lett.* **24**, 163.
- Lemons, R. A., and C. F. Quate, 1979, in *Physical Acoustics* Vol. 14, edited by W. P. Mason and R. N. Thurston (Academic, London), p. 1.
- Liang, K. K., S. D. Bennett, B. Khuri-Yakub, and G. S. Kino, 1985, *IEEE Trans. SU-32*, 266.
- Liang, K. K., G. S. Kino, and B. Khuri-Yakub, 1985, *IEEE Trans. SU-32*, 213.
- Love, A. E. H., 1911, *Some Problems of Geodynamics* (Cambridge University, Cambridge, England).
- Miller, A. J., 1985, *IEEE Trans. SU-32*, 320.
- Nagy, P. B., and L. Adler, 1990, *J. Appl. Phys.* **67**, 3876.
- Nedler, J. A., and R. Mead, 1965, *Computer J.* **7**, 308.
- Ocheltree, K. S., and L. A. Frizzel, 1989, *IEEE Trans. Ultrason. Ferroelect. Freq. Contr.* **36**, 242.
- Quate, C. F., 1980, in *Scanned Image Microscopy*, edited by E. A. Ash (Academic Press, London), p. 23.
- Quate, C. F., 1985, *IEEE Trans. SU-32*, 132.
- Quate, C. F., A. Atalar, and H. K. Wickramasinghe, 1979, *Proc. IEEE* **67**, 1092.
- Rayleigh, L., 1885, *Proc. Lond. Math. Soc.* **17**, 4.
- Richards, B., and E. Wolf, 1959, *Proc. R. Soc. London, Ser. A* **253**, 358.
- Rugar, D., 1981, Ph.D. thesis (Stanford University).
- Rugar, D., 1984, *J. Appl. Phys.* **56**, 1338.
- Schoch, A., 1950, *Ergebnisse exakt. Naturwiss.* **23**, 160.
- Schoch, A., 1952, *Acustica* **2**, 18.
- Scrubby, C. B., K. R. Jones, and L. Antoniazzi, 1987, *J. Nondestructive Evaluations* **5**, 145.
- Sezewa, K., and K. Kanai, 1935, *Bull. Earth. Res. Inst. Tokyo*, **13**, 237.
- Sheppard, C. J. R., and T. Wilson, 1981, *Appl. Phys. Lett.* **38**, 859.
- Smith, I. R., and H. K. Wickramasinghe, 1982, *Electron. Lett.* **18**, 955.
- Tamir, T., 1972, *Optik* **36**, 209.
- Thomson, W. T., 1950, *J. Appl. Phys.* **21**, 89.
- Tiersten, H. F., 1969, *J. Appl. Phys.* **40**, 770.
- Überall, H., 1973, in *Physical Acoustics* Vol. 10, edited by W. P. Mason and R. N. Thurston (Academic, New York), p. 1.
- Weglein, R. D., 1979a, *Appl. Phys. Lett.* **34**, 179.
- Weglein, R. D., 1979b, *Appl. Phys. Lett.* **35**, 215.
- Weglein, R. D., 1985, *IEEE Trans. SU-32*, 225.
- Weglein, R. D., 1987, *IEEE 1987 Ultrasonics Symposium Proceedings*, edited by B. R. McAvoy (IEEE, New York), Vol. 2, p. 823.
- Wickramasinghe, H. K., 1979, *J. Appl. Phys.* **50**, 664.
- Wilson, R. D., and R. D. Weglein, 1984, *J. Appl. Phys.* **55**, 3261.
- Yamanaka, K., 1982, *Electron. Lett.* **18**, 587.
- Yu, Z., 1991, Ph.D. thesis (University of Bremen, Germany).
- Yu, Z., and S. Boseck, 1991, *Optik* **88**, 73.
- Yu, Z., and S. Boseck, 1992, in *Acoustic Imaging* Vol. 19, edited by H. Ermert and H. P. Harjes (Plenum, New York/London), p. 617.
- Yu, Z., and S. Boseck, 1994, *Optik* **96**, 83.
- Yu, Z., and S. Boseck, 1995.
- Zemanek, J., 1971, *J. Acoust. Soc. Am.* **49**, 181.